Inorganic Chemistry

pubs.acs.org/IC

Article

Synthesis of Heterometallic Zirconium Alkoxide Single-Source Precursors for Bimetallic Oxide Deposition

Jonathan Slaughter, Chloe Coates, George Phillips, Dipanjana Choudhury, Andrew D. Bond, Clare P. Grey,* and Dominic S. Wright*

Cite This: *Inorg. Chem.* 2022, 61, 19203–19219

Read Online

ACCESS | Metrics & More | Article Recommendations | Supporting Information

ABSTRACT: Single-source precursors are ubiquitous in a number of areas of chemistry and material science due to their ease of use and wide range of potential applications. The development of new single-source precursors is essential in providing entries to new areas of chemistry. In this work, we synthesize nine new structurally related bimetallic metal-zirconium alkoxides, which can be used as single-source precursors to zirconia-based materials. Detailed analysis of the structures of these complexes provides important insights into the main factors influencing their aggregation. Investigation of the thermal decomposition of these species by TGA, PXRD, SEM, and EDS reveals that they can be used to produce bimetal oxides, such as Li_2ZrO_3, or a mixture of metal oxides, such as CuO and ZrO_2. Significantly, these studies show that thermodynamically unstable forms of zirconia, such as the tetragonal phase, can be stabilized by metal doping, providing the promise for targeted deposition of zirconia materials for specific applications.

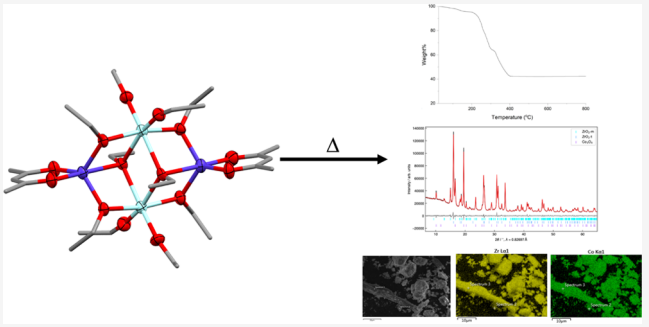

INTRODUCTION

Metal oxides are used extensively in a very broad range of applications in the modern world, such as in batteries,[1] solar cells,[2] catalysts,[3] and sensors.[4] The varied properties of metal oxides stem from complex factors associated with the bonding and electronic properties of the metals involved. For example, zirconium oxide is a hard ceramic used as an enamel,[5] whereas zinc oxide can act as a wide-band-gap semiconductor, which can be used in solar cells.[6] The combination of two different metals within the oxide to produce bimetallic oxides can lead to a large number of possible materials, which can combine the features of both metal components. Through the choice of specific metals, even greater specialization of applications can be achieved. This has recently been investigated in the use of protective coatings for battery electrodes, such as the use of $LiAlO_2$ coatings on cathodes. This bimetallic oxide coating can prevent degradation of the electrode due to its inert nature, similar to Al_2O_3, and also allows lithium diffusion through the coating, resulting in enhanced electrochemical performance compared to uncoated and Al_2O_3-coated cathodes.[7] Bimetallic oxides are also of interest in water splitting. For example, the bimetallic oxide $Fe_{1.89}Mo_{4.11}O_7$ was shown to be a highly efficient electrocatalyst for the hydrogen evolution reaction.[8] The other component of water splitting, the oxygen evolution reaction, has been shown to be catalyzed by MFe_2O_4 (M = Co, Ni, Cu, Mn), with all of these bimetallic oxides showing better catalytic performance than Fe_2O_3.[9] Even small amounts of another metal can strongly affect a monometallic oxide. For example, the doping of TiO_2 with transition metals has been widely investigated due to the reduction in the band gap upon doping, allowing the band gap to fall within the visible region and producing a high-performance photocatalyst.[10,11]

The area of single-source precursors (SSPs) is a well-established field in chemistry, with the ability to produce complex materials by thermal or chemically activated decomposition of a single-molecular species. Not surprisingly, this strategy has been used extensively for the deposition of functional films of metal oxides and mixed-metal oxides for a range of applications. Advantages of using SSPs in this setting include the possibility for lower temperature oxide deposition, greater atomic, compositional and morphological control of the deposited material, and the possibility of using high-throughput techniques (such as spray coating) for large-scale and large-area device manufacture.[12,13] Conventional routes to ceramic materials often require the use of oxides, nitrates, or carbonates, which require very high temperatures, especially if a product needs to be highly crystalline.[14] Developing areas of

Received: August 10, 2022
Published: November 16, 2022

research are the use of SSPs in the fabrication of multijunction water-splitting cells and in the synthesis of battery cathodes. A recent example of the use of an SSP is the production of nanostructured $BiVO_4$ photoanode films for water oxidation from the low-temperature decomposition of the vanadate cage compound $Bi_4(DMSO)_{12}V_{13}O_{40}H_3$. This method was shown to produce an even distribution of elements and, significantly, can be used to deposit large-area water-splitting devices.[15] The decomposition of $Ni_2Ti_2(OEt)_8(acac)_4$ (acac = acetylacetonate) was also shown to produce $NiTiO_3$, another valuable component for photooxidation of water.[16] In the battery field, the thermal decomposition of $LiCo(acac)_3$ was shown to produce crystalline $LiCoO_2$, a common lithium-ion battery cathode.[17]

Pertinent to the current work, zirconium alkoxides have been used extensively as SSPs for the production of zirconia films by solution hydrolysis or thermal decomposition. A particular area of interest has been the coating of the cathode material NMC811 ($LiNi_{0.8}Mn_{0.1}Co_{0.1}O_2$) for the next generation of high-energy-density lithium-ion batteries. Zirconia-coated NMC811 has shown enhanced electrochemical behavior due to the chemical inertness of the zirconia, which slows the decomposition of the cathode.[18] Additionally, zirconium alkoxides have been used to produce zirconia coatings on stainless steel sheets, improving their heat resistance against oxidation.[19]

The combination of zirconium alkoxides with other organometallic compounds has produced a number of heterometallic zirconium alkoxides, which can be used as SSPs for the production of metal-zirconium bimetallic oxides. For example, decomposition of the cobalt-zirconium species $CoZr_2(acac)_2(O^iPr)_8$ under autogenic pressure resulted in the formation of spherical ZrO_2 and Co particles, covered in carbon.[20] The thermal decomposition of the zinc-zirconium alkoxide $Zr_3Zn_7O(OH)_3(OR)_{15}Cl_6$ has also been shown to result in the formation of ZrO_2 crystallites on the surface of ZnO nanowires.[21] A further example is the SSP $[Cu_4Zr_2O_2(dmae)_4(OAc)_8]\cdot 2H_2O$ (dmae = *N*,*N*-dimethylaminoethanolato), which produced a $CuZrO_3$-CuO composite using aerosol-assisted chemical vapor deposition.[22] There are potentially a number of advantages of including transition metals into the zirconia coatings for battery applications, including modifying the ionic conductor behavior of the film and increasing the stability of the protective layer, potentially via substitution of the transition metals into the surface and subsurface layers of the (active) electrode material. However, so far, this area has not been explored in the literature.

A prerequisite for the systematic study of the effects of inclusion of other metal dopants into zirconia for battery applications is an array of available SSPs, which include different metals. While a number of heterometallic zirconium alkoxides have been synthesized previously,[23−25] in this work, we have prepared a wide range of new organically soluble heterometallic zirconium alkoxides, whose alkoxide peripheries should be readily hydrolyzed or thermolyzed to give metal-doped zirconia, bimetallic oxides, or a mixture of monometallic oxides. We explore their differing molecular structures systematically, which are highly dependent on the additional metal used, and investigate the decomposition of these materials into oxide phases. Overall, this study has generated a number of new zirconium-based SSPs which have the potential to be used in multiple areas of chemical deposition, and provides a first step to their applications in the battery area.

EXPERIMENTAL SECTION

General Procedures. All reactions were carried out under dry nitrogen, using a double-manifold vacuum line and a glovebox. Solvents were distilled over sodium (toluene) or sodium-potassium amalgam (THF and *n*-hexane) immediately before use. Anhydrous ethanol and *n*-propanol were purchased from Fisher Scientific and Alfa Aesar, respectively, and used as provided. Reagents were purchased from commercial suppliers (Sigma-Aldrich, Alfa Aesar, or Fisher Scientific) and used as provided. Reactions at −78 °C were achieved using a dry ice/acetone bath.

Solution NMR spectroscopic data were collected on either a Bruker Avance III HD 500 MHz Smart Probe NMR spectrometer or a Bruker Avance III HD 400 MHz NMR spectrometer. Spectra were obtained at 25 °C (unless otherwise stated) using deuterated solvents which were dried over molecular sieves (4 Å). For ^{1}H and ^{13}C NMR, chemical shifts are internally referenced to the deuterated solvent used and calculated relative to TMS.[26] For ^{7}Li and ^{27}Al NMR, the chemical shifts are referenced to 9.7 M LiCl in D_2O and 1.1 M $Al(NO_3)_3$ in D_2O, respectively. Chemical shifts are expressed in δ ppm. The following abbreviations are used: br = broad, m = multiplet, q = quartet, s = singlet, sext = sextet, t = triplet.

^{27}Al MAS NMR spectra were collected using a Hahn-echo pulse sequence ($\pi-\tau-2\pi-\tau$ acquisition with a recycle delay of 0.73 μs). The sample was loaded into a 2.5 mm rotor and the experiments were conducted at a magic-angle spinning (MAS) frequency of 20 kHz using a 500 MHz (11.8 T) spectrometer (Bruker Avance III). The spectrum was externally referenced against AlF_3 powder (−17 ppm) for ^{27}Al.

Elemental analysis of carbon and hydrogen was performed using a PerkinElmer 240 Elemental Analyser or an Exeter Analytical CE-440 Elemental Analyser. Inductively coupled plasma optical emission spectrometry (ICP-OES) was run and analyzed on a Thermo Fisher Scientific iCAP7400 Duo ICP-OES spectrometer using Qtegra software. ICP standards were purchased from Sigma-Aldrich and nitric acid (trace-metal grade) from Fisher. Samples were dissolved in nitric acid (5 mL) at room temperature, then diluted with water (5 mL). A 0.5 mL aliquot was diluted to 10 mL with water and then analyzed.

X-ray crystallographic data were collected using either a Nonius KappaCCD (Mo Kα) or Bruker D8-QUEST diffractometer equipped with an Incoatec IμS microsource (Cu Kα). The temperature was held at 180(2) K using an Oxford Cryosystems N_2 cryostat. Data integration and reduction were undertaken with HKL Denzo/Scalepack (Nonius) or with SAINT in the APEX3 software suite (Bruker). Multiscan corrections were applied using SORTAV (Nonius) or SADABS (Bruker). Structures were solved using SHELXT and refined using SHELXL.

Thermogravimetric analysis (TGA) of samples was performed on a Mettler Toledo TGA/DSC 2 STAR^e System. Samples of 10−20 mg were heated to 800 °C at a rate of 10 °C min^{-1}. Measurements on samples were performed under a constant flow (80 mL min^{-1}) of air (19−22% O_2 in N_2, <10 ppm H_2O), provided by Air Liquide UK Limited.

Infrared spectroscopy was carried out on a PerkinElmer Spectrum One FTIR Spectrometer fitted with a PerkinElmer ATR sampling accessory.

The UV−visible absorbance data were acquired on a VARIAN Cary 50 Bio UV−visible Spectrophotometer, using 0.01 M solutions of the complexes in *n*-hexane.

Synchrotron powder X-ray diffraction (PXRD) patterns of the decomposition products were collected on the I11 beamline at Diamond Light Source using an energy of approximately 15 keV (0.826 Å). The data were collected over multiple beamtimes and each time the wavelengths and instrumental parameters were refined against a Si standard; the wavelength used is indicated for each refinement. The PXRD data for complex **9** which had been heated to

https://doi.org/10.1021/acs.inorgchem.2c02852
Inorg. Chem. 2022, 61, 19203−19219

1000 °C were collected on a Malvern Panalytical Empyrean instrument, equipped with an X'celerator Scientific detector using non-monochromated Cu Kα radiation (1.5418 Å). Data were refined using Topas Academic v.6. For mixed-metal phases, the atomic displacement parameters were constrained to be the same. Since there is a strong correlation between the atomic displacement parameters and occupancies of different atoms, the degree of cation mixing in the cubic and tetragonal phases is considered not to be fully quantitative and is simply taken as an indication of doping stabilizing the higher-symmetry phases. For this reason, some of the elemental compositions do not follow the expected M/Zr 1:1 ratio (e.g., Fe, Co, Mg, and Ni), but the accuracy is sufficient to infer the phases present, so the refinements were not constrained further.

To investigate the size and structure of the powder particles, elemental distribution, scanning electron microscopy (SEM), and energy-dispersive X-ray spectroscopy (EDS) were used, employing a "TESCAN MIRA3" microscope. To fix the samples on the sample holders, a small amount of the powders were sprinkled onto graphite tapes, which were then sputtered with 10 nm thick chromium to improve conductivity and allow images to be taken. EDS analysis was performed with an X-MAX 150 mm^2 detector (from Oxford Instruments) and processed with AZTEC software to produce maps of the elemental distributions. The accelerating voltage for these measurements was set to 20 kV.

Synthesis of $Li_2Zr_2(O^nPr)_{10}(THF)_2$ (1). $Zr(O^nPr)_4$ (70 wt % in *n*-propanol, 0.90 mL, 2 mmol) and *n*-hexane (5 mL) were combined and cooled to −78 °C. ^{n}BuLi (1.6 M in *n*-hexanes, 1.25 mL, 2 mmol) was added dropwise, and the resulting solution was left to warm up to room temperature over the course of 2 h, producing a white suspension. The solvent was removed under vacuum, and the resulting white solid residue was dissolved in THF (0.5 mL). Storage of the solution at −20 °C for 16 h resulted in the formation of transparent crystals of **1** (290 mg, 31%). Elemental analysis calculated (%) for $C_{38}H_{86}Li_2O_{12}Zr_2$: C 49.0, H 9.3. Found: C 46.2, H 9.1. ^{1}H NMR spectroscopy (400 MHz, C_6D_6): δ 4.38−4.11 (20 H, m, OCH_2), 3.69 (7.5 H, m, THF), 2.12−1.69 (20 H, m, CH_2), 1.40 (7.5 H, m, THF), 1.22−0.98 (30 H, m, Me). ^{13}C NMR spectroscopy (101 MHz, C_6D_6): δ 71.3, 70.0, 69.9 (OCH_2), 68.3 (THF), 29.0, 28.8, 26.7 (CH_2), 25.5 (THF), 11.2, 11.0, 10.4 (Me). ^{7}Li NMR spectroscopy (155 MHz, C_6D_6): δ 0.6, 0.3.

Synthesis of $Mg_2Zr_2(O^nPr)_{12}(^nPrOH)_4$ (2). $Zr(O^nPr)_4$ (70 wt % in *n*-propanol, 3.6 mL, 8 mmol), *n*-propanol (2 mL), and *n*-hexane (20 mL) were combined and cooled to −78 °C. $^nBu_2Mg$ (1.0 M in *n*-heptane, 8 mL, 8 mmol) was added dropwise, and the resulting solution was left to warm up to room temperature overnight, producing a white suspension. The suspension was dissolved by gently heating the solvent. Storage of the solution at −20 °C for 16 h resulted in the formation of transparent crystals of **2** (3.30 g, 70%). Elemental analysis calculated (%) for $C_{48}H_{116}Mg_2O_{16}Zr_2$: C 48.8, H 9.9. Found: C 49.4, H 10.1. ^{1}H NMR spectroscopy (400 MHz, C_6D_6): δ 4.68 (4 H, s br, OH), 4.32−4.02 (24 H, m, OCH_2), 3.53 (8 H, t, J = 7.0 Hz, OCH_2), 1.97 (24 H, m, CH_2), 1.55 (8 H, sext, J = 7.0 Hz, CH_2), 1.10 (36 H, m, Me), 0.85 (12 H, t, J = 7.0 Hz, Me). ^{13}C NMR spectroscopy (101 MHz, C_6D_6): δ 69.9, 64.9 (OCH_2), 28.6, 26.8 (CH_2), 11.0, 10.8, 10.5, 10.4, 10.3 (Me).

Synthesis of $Co_2Zr_2(OEt)_{10}(acac)_2$ (3). $Zr(OEt)_4$ (1.09 g, 4 mmol), $Co(acac)_2$ (514 mg, 2 mmol), and toluene (5 mL) were heated to reflux for 1 h, producing a purple solution. The toluene was removed under vacuum, and the resulting purple solid was redissolved in *n*-hexane (5 mL) with heating. Slow cooling of the solution to room temperature for 16 h resulted in the formation of purple crystals of **3** (540 mg, 57% wrt $Co(acac)_2$). Elemental analysis calculated (%) for $C_{30}H_{64}Co_2O_{14}Zr_2$: C 38.0, H 6.8. Found: C 37.6, H 6.8.

Synthesis of $Ni_2Zr_2(OEt)_8(acac)_4$ (4). $Zr(OEt)_4$ (1.09 g, 4 mmol), $Ni(acac)_2$ (514 mg, 2 mmol), and toluene (5 mL) were heated to reflux for 1 h, producing a green solution and a small amount of green solid. The solid was removed by filtration. The solution was concentrated to about 3 mL under vacuum. Storage of the material at −30 °C for 16 h resulted in the formation of green crystals of **4** (430 mg, 41% wrt $Ni(acac)_2$). Elemental analysis calculated (%) for $C_{36}H_{68}Ni_2O_{16}Zr_2$: C 40.9, H 6.5. Found: C 40.7, H 6.6.

Synthesis of $Fe_2Zr_2(OEt)_{10}(acac)_2$ (5). $Zr(OEt)_4$ (1.09 g, 4 mmol), $FeCl_2$ (507 mg, 4 mmol), KOEt (673 mg, 8 mmol), ethanol (2 mL), and toluene (10 mL) were heated to reflux for 2 h, producing a dark green solution and a white solid. Acetylacetone (0.41 mL, 4 mmol) was added, which turned the solution red, and the suspension was stirred for 1 h. The solvent was removed under vacuum and *n*-hexane (10 mL) was added. The white solid was removed by filtration, and the solution was concentrated to about 3 mL under vacuum. Storage of the solution at −20 °C for 16 h resulted in the formation of red crystals of **5** (365 mg, 19%). Elemental analysis calculated (%) for $C_{30}H_{64}Fe_2O_{14}Zr_2$: C 38.2, H 6.8. Found: C 35.9, H 6.6.

Synthesis of $Cu_2Zr_2(OEt)_{10}(acac)_2$ (6). $Zr(OEt)_4$ (1.09 g, 4 mmol), $Cu(acac)_2$ (524 mg, 2 mmol), $CuCl_2$ (269 mg, 2 mmol), KOEt (337 mg, 4 mmol), ethanol (2 mL), and toluene (10 mL) were heated to reflux for 2 h, producing a dark blue solution and a white solid. The white solid was removed by filtration, and the solvent was then removed under vacuum. The resulting blue residue was dissolved in *n*-hexane (2 mL). Storage of the solution at −30 °C for 16 h resulted in the formation of blue crystals of **6** (535 mg, 28%). Elemental analysis calculated (%) for $C_{30}H_{64}Cu_2O_{14}Zr_2$: C 37.6, H 6.7. Found: C 37.6, H 6.7.

Synthesis of $Mn_{1.67}Zr_{2.33}(OEt)_{10.66}(acac)_2(EtOH)_{1.34}$ (7). $Zr(OEt)_4$ (1.09 g, 4 mmol), $MnCl_2$ (503 mg, 4 mmol), KOEt (673 mg, 8 mmol), ethanol (2 mL), and *n*-hexane (10 mL) were heated to reflux for 2 h, producing an orange solution and a white solid. Acetylacetone (0.41 mL, 4 mmol) was added, and the suspension was stirred for 1 h. The white solid was removed by filtration and storage of the solution at −20 °C for 16 h, resulting in the formation of brown crystals of **7** (365 mg, 20% wrt $Zr(OEt)_4$). Elemental analysis calculated (%) for $C_{34}H_{75.34}Mn_{1.67}O_{16}Zr_{2.33}$: C 39.1, H 7.3, Mn 8.8, Zr 20.4. Found: C 39.0, H 7.6, Mn 10.4, Zr 20.0.

Synthesis of $Zn_2Zr_2(OEt)_{10}(acac)_2$ (8). $Zr(OEt)_4$ (1.09 g, 4 mmol), $ZnCl_2$ (545 mg, 4 mmol), KOEt (673 mg, 8 mmol), ethanol (2 mL), and toluene (10 mL) were heated to reflux for 2 h, producing a yellow solution and a white solid. Acetylacetone (0.41 mL, 4 mmol) was added, and the suspension was stirred for 1 h. The solvent was removed under vacuum, and *n*-hexane (10 mL) was added. The white solid was removed by filtration. Storage of the solution at −20 °C for 16 h resulted in the formation of colorless crystals of **8** (1.00 g, 52%). Elemental analysis calculated (%) for $C_{30}H_{64}O_{14}Zn_2Zr_2$: C 37.4, H 6.7. Found: C 37.4, H 6.7. ^{1}H NMR spectroscopy (400 MHz, C_6D_6): δ 5.19 (2 H, s, CH), 4.69 (4 H, q, J = 7.0 Hz, CH_2), 4.33 (8 H, q, J = 6.9 Hz, CH_2), 4.24 (8 H, q, J = 6.9 Hz, CH_2), 1.82 (12 H, s, Me_{acac}), 1.73 (6 H, t, J = 7.0 Hz, Me), 1.46 (12 H, t, J = 6.9 Hz, Me), 1.33 (3 H, t, J = 6.9 Hz, Me). ^{13}C NMR spectroscopy (101 MHz, C_6D_6): δ 193.5 (C═O), 99.7 (CH), 65.5, 65.0, 64.1 (CH_2), 28.1 (Me_{acac}), 20.4, 19.4, 19.2 (Me).

Synthesis of $Al_2Zr_2(OEt)_{10}(acac)_4$ (9). $Zr(OEt)_4$ (1.09 g, 4 mmol), $Al(OEt)_3$ (649 mg, 4 mmol), acetylacetone (0.82 mL, 8 mmol), and toluene (5 mL) were heated to reflux for 30 min, producing a gray suspension. The suspension was filtered through Celite to give a yellow solution. The solvent was removed under vacuum, and the resulting yellow solid was redissolved in *n*-hexane (5 mL). Storage of the solution at −30 °C for 16 h resulted in the formation of colorless crystals of **9** (818 mg, 38%). Elemental analysis calculated (%) for $C_{40}H_{78}Al_2O_{18}Zr_2$: C 44.3, H 7.2 Found: C 43.8, H 7.4. ^{1}H NMR spectroscopy (400 MHz, C_6D_6): δ 5.44−5.15 (4 H, m, CH), 4.94−3.62 (20 H, m, CH_2), 2.00−0.86 (54 H, m, Me). ^{13}C NMR spectroscopy (101 MHz, C_6D_6): δ 191.9, 190.2, 189.8 (C═O), 100.5 (CH), 65.6, 61.5, 61.1, 60.3 (CH_2), 32.0, 26.9, 26.4, 26.3, 26.2 (Me_{acac}), 23.1, 21.1, 20.4, 18.9, 18.8, 14.3 (Me). ^{27}Al NMR spectroscopy (104 MHz, C_6D_6): δ 34.3, 5.0.

RESULTS AND DISCUSSION

Synthesis and Structural Analysis. A total of nine new heterometallic zirconium alkoxides were synthesized in the

https://doi.org/10.1021/acs.inorgchem.2c02852
Inorg. Chem. 2022, 61, 19203−19219

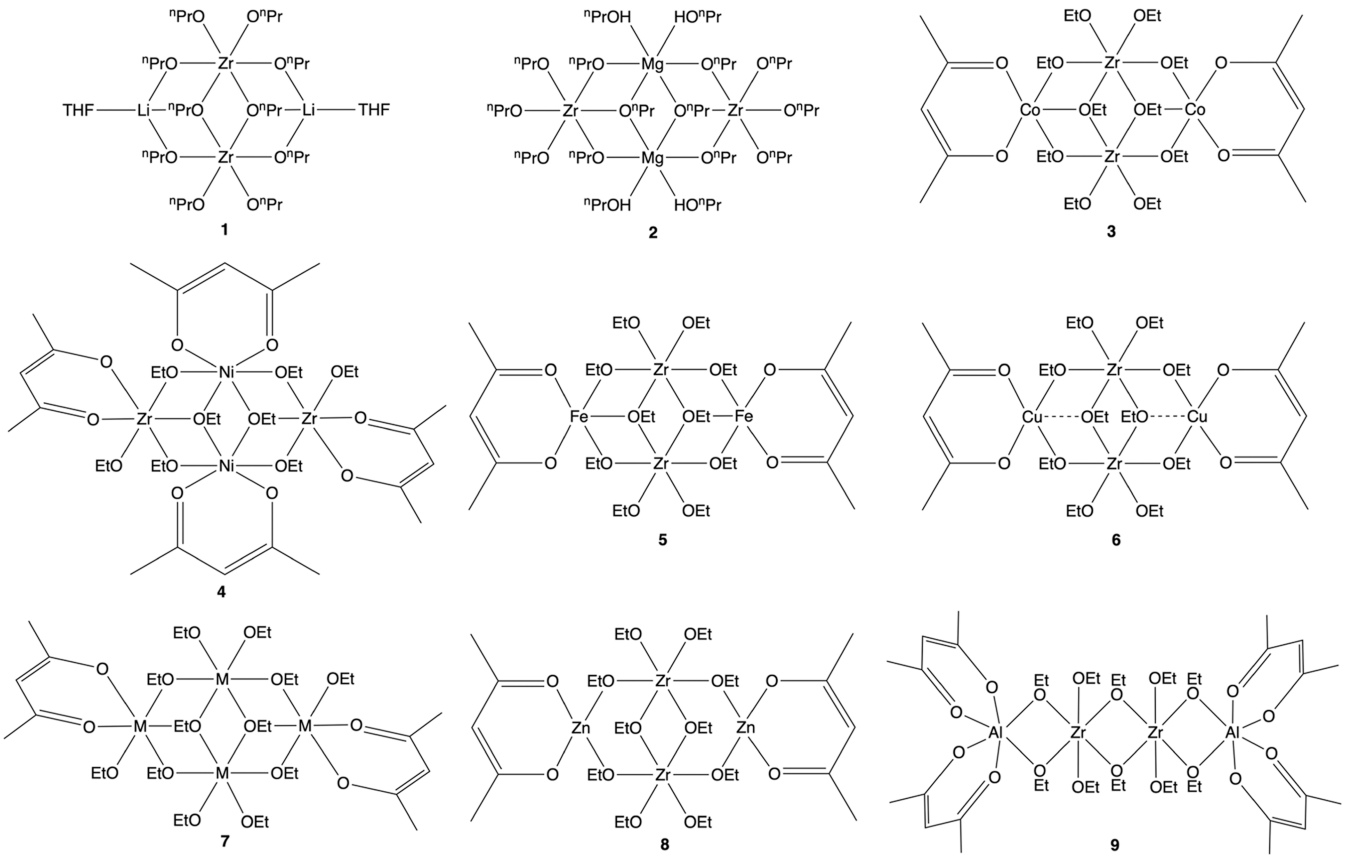

Figure 1. Structures of complexes **1**−**9**. Complex **7** has disorder of Zr and Mn at M sites.

current work (Figure 1). A summary of the synthetic approaches involved is shown in the SI (Scheme S1).

Initial studies in this work focused on the synthesis of a lithium-zirconium alkoxide species which could act as a lithium-zirconium oxide SSP. The 1:1 reaction of ^{n}BuLi with $Zr(O^{n}Pr)_4$ in *n*-propanol and *n*-hexane resulted in the formation of a white solid which was insoluble in *n*-hexane and toluene but proved very soluble in THF. Storage of a THF solution at −20 °C resulted in the formation of the crystalline material $Li_2Zr_2(O^{n}Pr)_{10}(THF)_2$ (**1**). The X-ray diffraction structure reveals a centrosymmetric molecule containing two lithium ions and two zirconium ions (Figure 2). From a chemical viewpoint, the structure can be seen as being composed of a $[\{(^{n}PrO)_4Zr(\mu_2\text{-}O^{n}Pr)\}_2]^{2-}$ dianion which coordinates two THF-coordinated Li^+ cations. This model and similar models discussed in this paper are based on the more covalent/directional nature of the Zr−O bonding, therefore making it the "dominant" fragment in these complexes in terms of its structural influence.[27] Compound **1** is isostructural with the previously reported complex $Li_2Zr_2(O^{i}Pr)_8(OMe)_2(THF)_2$.[28] The lithium ions have a distorted tetrahedral coordination geometry with one μ_3-*n*-propoxide, two μ_2-*n*-propoxides, and one THF. The zirconium ions have a distorted octahedral coordination geometry with two μ_3-*n*-propoxides, two μ_2-*n*-propoxides, and two terminal *n*-propoxides. Structurally, it is useful to take a polyhedral view of the coordination environments (see the SI). The central $\{Zr_2O_{10}\}$ core of the complex comprises a pair of ZrO_6 octahedra sharing one edge, with idealized point symmetry D_{2h}. The Li^+ cations define tetrahedra which attach to the $\{Zr_2O_{10}\}$ core through one of their triangular faces (actually sharing one edge with each of the ZrO_6 octahedra, see the SI) so that the point symmetry of the resulting $\{Zr_2Li_2O_{12}\}$ unit is reduced to C_{2h}.

Both NMR spectroscopy and elemental analysis suggested fewer than two equivalents of THF present in the dried crystalline material (1.9 by ^{1}H NMR spectroscopy and 1.0 by elemental analysis). It therefore appears that some of the coordinated THF is lost during drying of the crystalline material under vacuum prior to isolation and analysis. The ^{1}H NMR spectrum of **1** (Figure S1) reveals a complex pattern of peaks, with ratios that do not correspond to the solid-state structure. Cooling the sample to −50 °C did not result in significant resolution of the ^{1}H NMR spectrum (Figure S11), suggesting that in solution, **1** is in complex equilibrium with other species. This is also suggested by the ^{7}Li NMR spectrum where two peaks are present (Figure S3).

The next target was the synthesis of a magnesium-zirconium alkoxide. This was achieved through the 1:1 reaction of $^{n}Bu_2Mg$ with $Zr(O^{n}Pr)_4$ in *n*-propanol and *n*-hexane, with storage at −20 °C producing crystals of $Mg_2Zr_2(O^{n}Pr)_{12}(^{n}PrOH)_4$ (**2**). The solid-state structure of **2** (Figure 3) is isostructural with the previously reported ethoxide complex $Mg_2Zr_2(OEt)_{12}(EtOH)_4$[29] and can be regarded as resulting from the coordination of two bis-^{n}PrOH coordinated Mg^{2+} cations by two $[Zr(O^{n}Pr)_6]^{2-}$ dianions. The presence of ^{n}PrOH groups is confirmed in the IR spectrum of **2** (Figure S15), which shows a weak and broad O−H stretching band at ca. 3100 cm^{-1}. Molecules of **2** and previously reported $Mg_2Zr_2(OEt)_{12}(EtOH)_4$ both have a M_4O_{16} core which is prevalent in group IV alkoxides, such as titanium ethoxide.[30] From a polyhedral viewpoint, the M_4O_{16}

https://doi.org/10.1021/acs.inorgchem.2c02852
Inorg. Chem. 2022, 61, 19203−19219

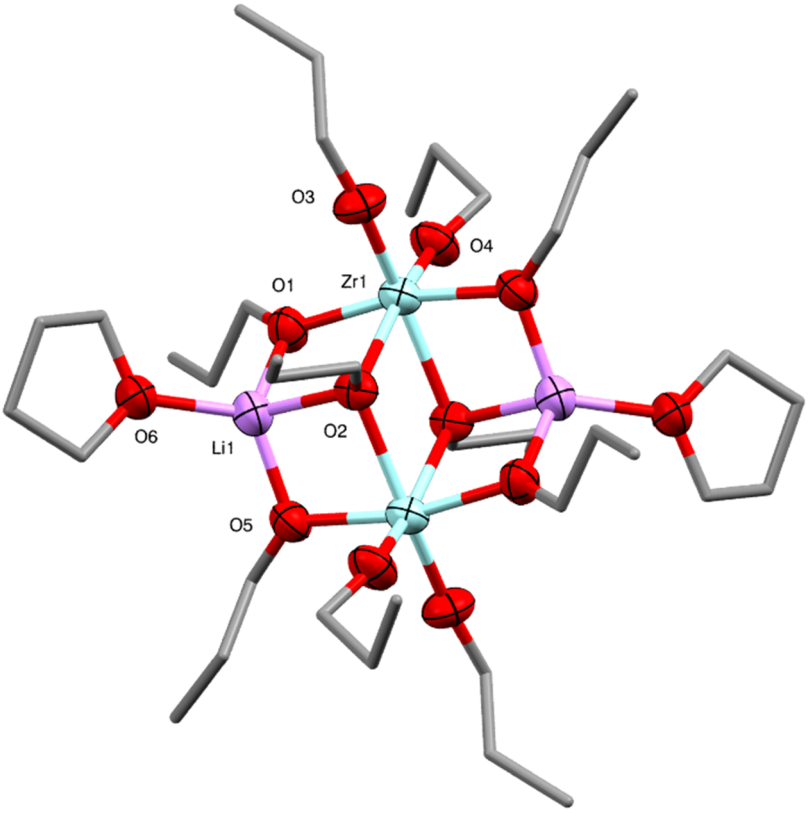

Figure 2. Molecular structure of $Li_2Zr_2(O^nPr)_{10}(THF)_2$ (**1**) (ellipsoids at 50% probability) with H atoms and minor disorder of some *n*-propoxide ligands omitted. Selected bond lengths (Å) and angles (°): Li1−O1 1.871(7), Li1−O2 2.087(8), Li1−O5 1.860(7), Li1−O6 1.950(7), Zr1−O1 2.070(3), Zr1−O2 2.247(2), Zr1−O2′ 2.249(2), Zr1−O3 1.940(3), Zr1−O4 1.951(3), Zr1−O5′ 2.084(3), O−Li1−O 88.3(3)-127.6(4), O−Zr1−O 70.37(9)-103.18(12).

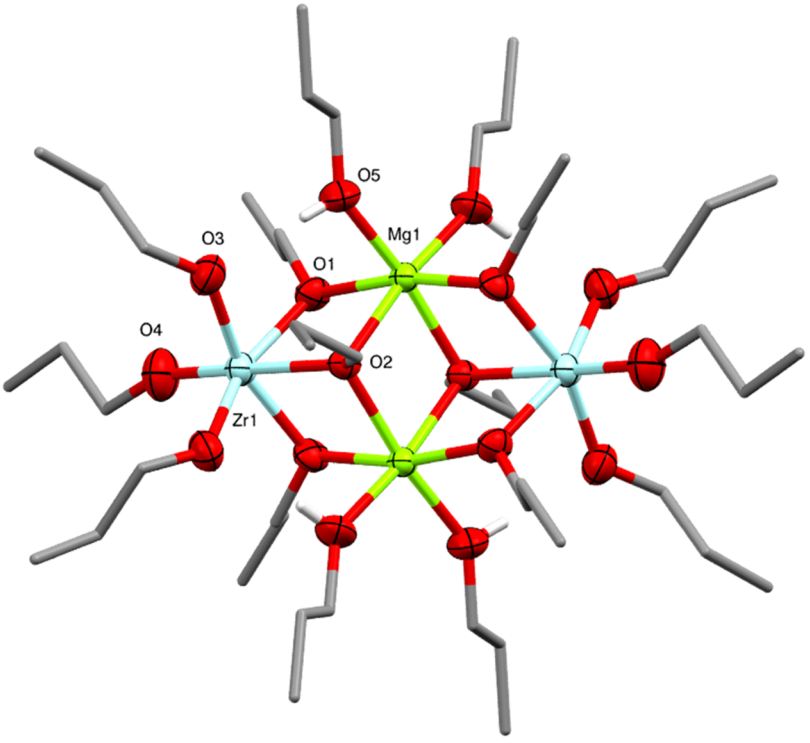

Figure 3. Molecular structure of $Mg_2Zr_2(O^nPr)_{12}(^nPrOH)_4$ (**2**) (ellipsoids at 50% probability) with H atoms and minor disorder of some *n*-propoxide ligands omitted. The O−H hydrogens of coordinating alcohols are shown. Selected bond lengths (Å) and angles (°): Mg1−O1 2.030(5), Mg1−O2 2.183(6), Mg1−O5 2.061(6), Zr1−O1 2.129(6), Zr1−O2 2.201(7), Zr1−O3 2.043(7), Zr1−O4 1.930(9), O−Li1−O 88.3(3)-127.6(4), O−Zr1−O 76.14(19)−99.9(4).

https://doi.org/10.1021/acs.inorgchem.2c02852
Inorg. Chem. 2022, 61, 19203−19219

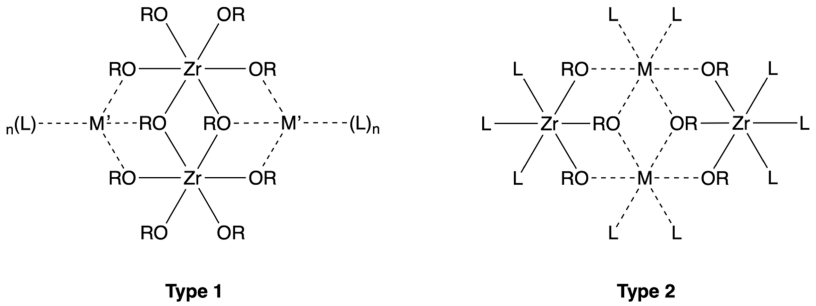

Figure 4. Two observed complex arrangements, type 1 containing a $[\{(RO)_4Zr(\mu_2\text{-}OR)\}_2]^{2-}$ dianion and with the coordinated metal ions (M′) at the peripheral sites, and type 2 containing $[Zr(OR)_6]^{2-}$ or $[Zr(OR)_4(acac)]^-$ anions and with the coordinated metal ions (M) at the center of the complex.

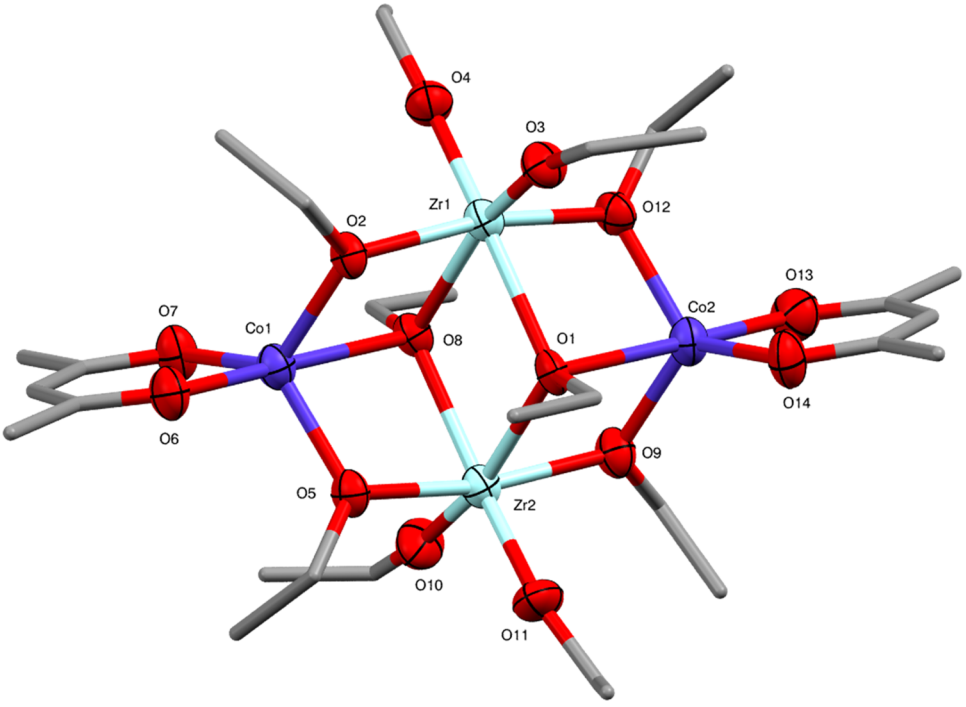

Figure 5. Molecular structure of $Co_2Zr_2(OEt)_{10}(acac)_2$ (**3**) (ellipsoids at 50% probability) with H atoms omitted. One representative molecule from the asymmetric unit is shown. The other molecule has essentially identical conformation. Selected bond lengths (Å) and angles (°): Co1−O2 1.957(6), Co1−O5 1.951(7), Co1−O6 2.015(8), Co1−O7 1.952(7), Co1−O8 2.404(6), Co2−O1 2.405(6), Co2−O9 1.953(7), Co2−O12 1.961(7), Co2−O13 2.001(8), Co2−O14 1.952(8), Zr1−O1 2.247(7), Zr1−O2 2.125(6), Zr1−O3 1.924(6), Zr1−O4 1.935(7), Zr1−O8 2.229(6), Zr1−O12 2.114(7), Zr2−O1 2.223(6), Zr2−O5 2.123(6), Zr2−O8 2.237(7), Zr2−O9 2.116(7), Zr2−O10 1.929(7), Zr2−O11 1.930(7), O−Co1−O 76.4(2)-125.2(3), O−Co2−O 76.5(3)-123.6(3), O−Zr1−O 69.7(2)-103.4(3), O−Zr2−O 69.9(2)−104.3(3).

structure comprises a pair of edge-sharing MgO_6 octahedra, with two ZrO_6 octahedra attached through one triangular face in the same manner as the LiO_4 tetrahedra in **1**. The fact that Zr^{4+} occupies the central octahedral sites (denoted the M sites, see Figure 4) in **1**, but outer octahedral sites (denoted the M′ sites, see Figure 4) in **2** indicate that the coordination requirements and ionic radii of the metal cations (Li^+ vs Mg^{2+}) have a key influence. Quantitative measures of the coordination environments (see Table S2) indicate that the central ZrO_6 octahedra in **1** are significantly more distorted from regular octahedral geometry compared to the central MgO_6 octahedra in **2**. The possibility to form more regular octahedral geometry in the central M sites may be a driving force for Mg^{2+} to preferentially occupy these sites (see also the discussion for Ni^{2+} in **4**).

In contrast to the lability of the THF ligands in **1**, NMR spectroscopy and elemental analysis suggest the retention of the *n*-propanol ligands in **2**. However, similarly to **1** the ^1H NMR spectrum of **2** (Figure S4) is more complex than the solid-state structure, suggesting multiple species or fluxionality in solution. Similar to **1**, cooling to −50 °C did not significantly resolve the ^1H NMR spectrum (Figure S12).

Further studies using the same synthetic methodology involving reactions of $Zr(O^nPr)_4$ with a range of transition-metal halides and potassium alkoxides proved unsuccessful, often producing intractable residues and no crystalline materials that could be characterized. Previous studies had, however, shown that the use of metal acetylacetonates as precursors in these reactions might be more successful.[23] The addition of acetylacetonate ligands can lead to compounds with decreased solubility and greater stability to hydrolysis.[31] Additionally, it was found that replacing $Zr(O^nPr)_4$ with $Zr(OEt)_4$ resulted in better crystallinity of the isolated compounds, making them amenable to X-ray analysis. The

https://doi.org/10.1021/acs.inorgchem.2c02852
Inorg. Chem. 2022, 61, 19203−19219

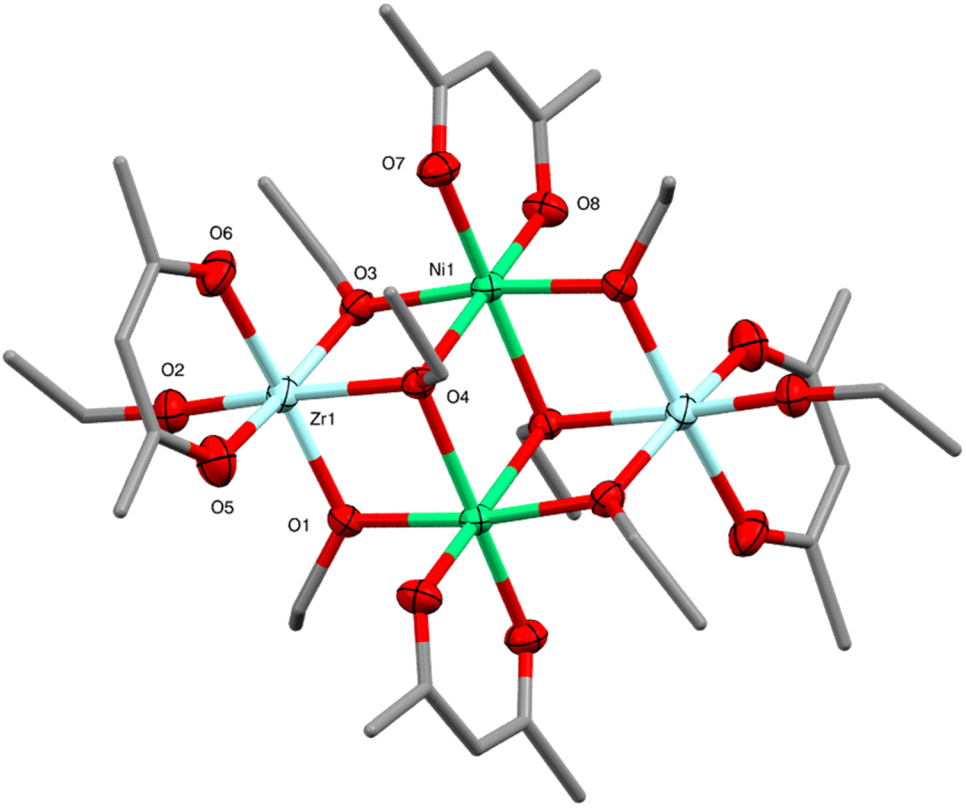

Figure 6. Molecular structure of $Ni_2Zr_2(OEt)_8(acac)_4$ (**4**) (ellipsoids at 50% probability) with H atoms omitted. Selected bond lengths (Å) and angles (°): Ni1−O1 2.0527(14), Ni1−O3 2.0698(14), Ni1−O4 2.1600(13), Ni1−O4′ 2.1892(13), Ni1−O7 1.9876(14), Ni1−O8 2.0016(14), Zr1−O1 2.0430(14), Zr1−O2 1.9270(15), Zr1−O3 2.0319(14), Zr1−O4 2.1866(13), Zr1−O5 2.1601(16), Zr1−O6 2.1676(15), O−Ni1−O 79.54(5)−96.12(5), O−Zr1−O 77.53(7)−97.10(6).

2:1 stoichiometric reaction of $Zr(OEt)_4$ and $Co(acac)_2$ in toluene heated to reflux resulted in the formation of $Co_2Zr_2(OEt)_{10}(acac)_2$ (**3**) as a blue crystalline solid. Molecules of **3** are isostructural with the previously reported compounds $Co_2Zr_2(O^nPr)_{10}(acac)_2$[32] and $Co_2Zr_2(O^iPr)_6(O^nPr)_4(acac)_2$,[23] which were synthesized in a similar manner to **3**. From the reaction stoichiometry, it is assumed that $Zr(OEt)_3(acac)$ is also formed as a side-product, which is more soluble in *n*-hexane than **3** and is therefore retained in solution during the crystallization step (Scheme S1). X-ray crystallography reveals two chemically similar, but crystallographically independent molecules in the lattice (one of which is shown in Figure 5). The overall structure of **3** is similar to that of **1**, being composed of a $[\{(EtO)_4Zr(\mu_2\text{-}OEt)\}_2]^{2-}$ dianion that coordinates two $[Co(acac)]^+$ fragments at the periphery of the $Zr_2Co_2O_6$ core. The high-spin d^7 Co^{2+} ions adopt a distorted trigonal-bipyramidal geometry, coordinated by one μ_3-ethoxide, two μ_2-ethoxides, and one acetylacetonate ligand. The average bond length to the μ_3-ethoxide is significantly longer than the other Co−O bonds (2.405 Å, cf. 1.956 Å for the μ_2-ethoxides). As in **1**, the Zr^{4+} ions are situated in the central M sites and have a distorted octahedral geometry, coordinated by two μ_3-ethoxides, two μ_2-ethoxides, and two terminal ethoxides. Quantitative measures (see Table S2) show that the distortion of the ZrO_6 octahedra from regular geometry is the greatest of any of the compounds in this paper. From the polyhedral viewpoint, the CoO_5 trigonal bipyramids are again attached to the central core through one of their triangular faces.

The same reaction using $Ni(acac)_2$ instead of $Co(acac)_2$ gave the complex $Ni_2Zr_2(OEt)_8(acac)_4$ (**4**). Interestingly, as shown by X-ray crystallography the centrosymmetric arrangement of this complex resembles that of **2**. Here, however, the $[Zr(O^nPr)_6]^{2-}$ dianions of **2** are replaced by $[Zr(OEt)_4(acac)]^-$ monoanions, in which two of the alkoxide ligands are substituted for a monoanionic acetylacetonate ligand. The $[Zr(OEt)_4(acac)]^-$ anions of **4** coordinate two $[Ni(acac)]^+$ fragments at the center of the core (Figure 6). This arrangement gives the high-spin d^8 Ni^{2+} ions a distorted octahedral geometry (being coordinated by two μ_3-ethoxides, two μ_2-ethoxides and chelated by an acetylacetonate ligand) and is isostructural with the previously reported nickel-titanium alkoxide complex $Ni_2Ti_2(OEt)_8(acac)_4$, which was obtained from the reaction of $Ni(acac)_2$ with $Ti(OEt)_4$.[33] As seen for **2**, the Ni^{2+} ions in the central M sites show the most regular octahedral geometry of any complex in this paper (see Table S2), suggesting again that the occupation of the M vs the M′ sites may be influenced by the possibility for Ni^{2+} to form a more regular octahedral geometry in the M sites.

Rather than using the preformed metal acetylacetonate precursors themselves, it was found that the acetylacetonate ligands could also be incorporated into the mixed-metal complexes using an in situ approach. Heating a 1:1:2 stoichiometric mixture of $Zr(OEt)_4$, $FeCl_2$, and KOEt to reflux in toluene and ethanol, followed by the addition of one equivalent of acetylacetone (acacH) produced crystals of $Fe_2Zr_2(OEt)_{10}(acac)_2$ (**5**) after workup. If no acetylacetone is added to the reaction an intractable red residue is formed, presumably of $Fe_2Zr_2(OEt)_{12}$. The addition of acetylacetone

https://doi.org/10.1021/acs.inorgchem.2c02852
Inorg. Chem. 2022, 61, 19203−19219

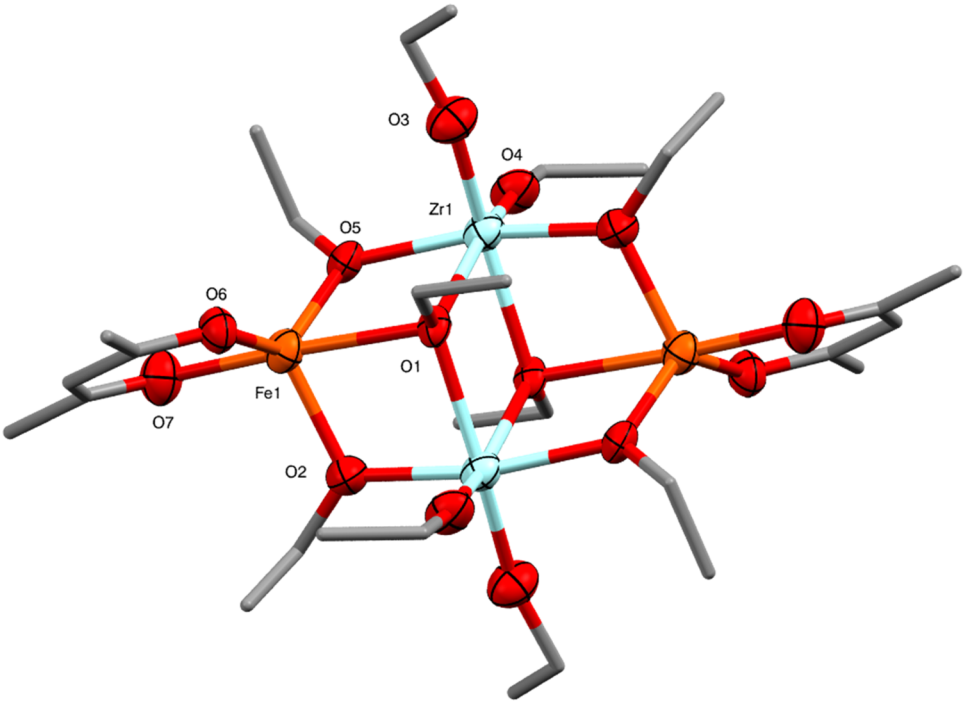

Figure 7. Molecular structure of $Fe_2Zr_2(OEt)_{10}(acac)_2$ (**5**) (ellipsoids at 50% probability) with H atoms omitted. One representative molecule from the asymmetric unit is shown. The other molecule has essentially identical conformation. Selected bond lengths (Å) and angles (°): Fe1−O1 2.419(7), Fe1−O2 2.030(9), Fe1−O5 1.989(8), Fe1−O6 1.945(9), Fe1−O7 2.029(10), Zr1−O1 2.250(8), Zr1−O2 2.098(9), Zr1−O3 1.926(8), Zr1−O4 1.915(8), Zr1−O5 2.129(8), O−Fe1−O 75.9(3)-130.3(4), O−Zr1−O 70.4(3)−103.9(4).

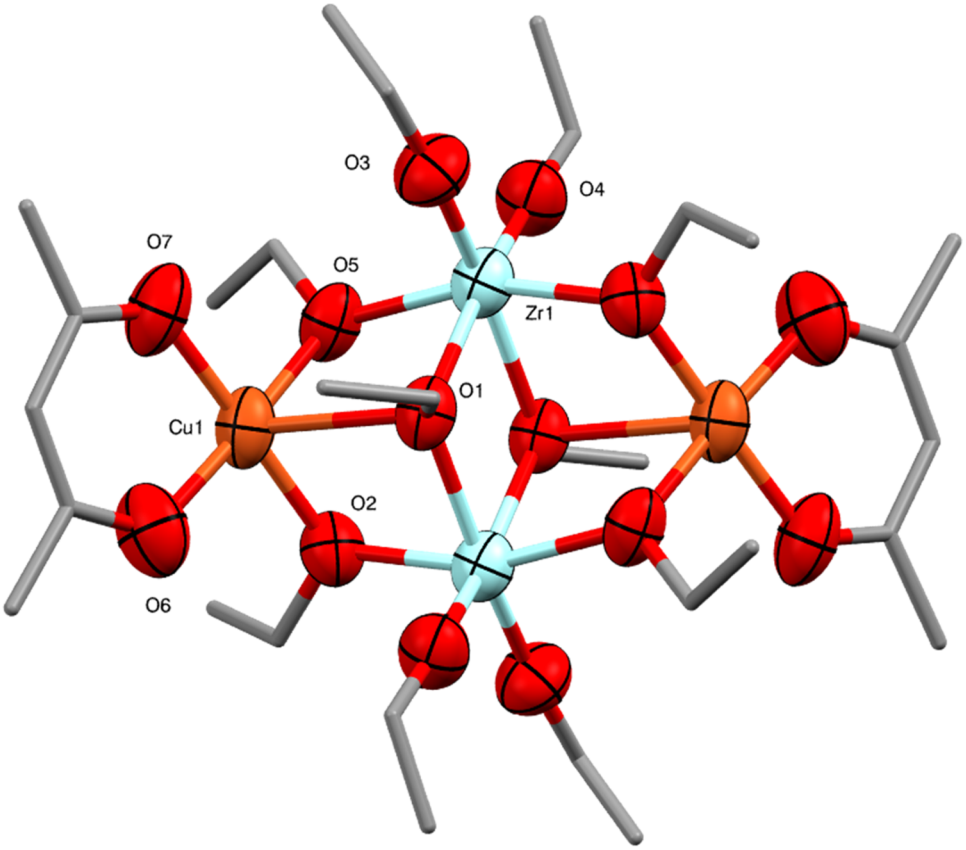

Figure 8. Molecular structure of $Cu_2Zr_2(OEt)_{10}(acac)_2$ (**6**) (ellipsoids at 50% probability) with H atoms and minor disorder of one ethoxide ligand omitted. Selected bond lengths (Å) and angles (°): Cu1−O1 2.543(3), Cu1−O2 1.959(4), Cu1−O5 1.964(4), Cu1−O6 1.914(5), Cu1−O7 1.918(4), Zr1−O1 2.212(4), Zr1−O1′ 2.205(4), Zr1−O2 2.116(4), Zr1−O3 1.936(4), Zr1−O4 1.933(4), Zr1−O5 2.131(4), O−Cu1−O 74.4(2)-111.3(2), O−Zr1−O 73.62(13)-101.0(2).

https://doi.org/10.1021/acs.inorgchem.2c02852
Inorg. Chem. 2022, 61, 19203−19219

Table 1. Calculated Crystal Field Stabilization Energies (CFSE) for Octahedral, Tetrahedral, Square Pyramidal, and Trigonal-Bipyramidal Geometries of the High-Spin Metal Ions, and the Observed Structure and Ionic Radius of the Ion

	CFSE					
	octahedral	tetrahedral	square pyramidal	trigonal-bipyramidal	observed structure	ionic radius (pm)
1 Li^{+} (d^0)	0	0	0	0	type 1 (tet)	90
2 Mg^{2+} (d^0)	0	0	0	0	type 2 (oct)	86
3 Co^{2+} (d^7)	$-0.8\Delta_o$	$-0.53\Delta_o$	$-0.91\Delta_o$	$-0.54\Delta_o$	type 1 (tbp)	88.5
4 Ni^{2+} (d^8)	$-1.2\Delta_o$	$-0.36\Delta_o$	$-1.00\Delta_o$	$-0.63\Delta_o$	type 2 (oct)	83
5 Fe^{2+} (d^6)	$-0.4\Delta_o$	$-0.27\Delta_o$	$-0.46\Delta_o$	$-0.27\Delta_o$	type 1 (tbp)	92
6 Cu^{2+} (d^9)	$-0.6\Delta_o$	$-0.18\Delta_o$	$-0.91\Delta_o$	$-0.71\Delta_o$	type 1 (sbp)	87
7 Mn^{2+} (d^5)	0	0	0	0	mixed-metal sites	97
8 Zn^{2+} (d^{10})	0	0	0	0	type 1 (tet)	88

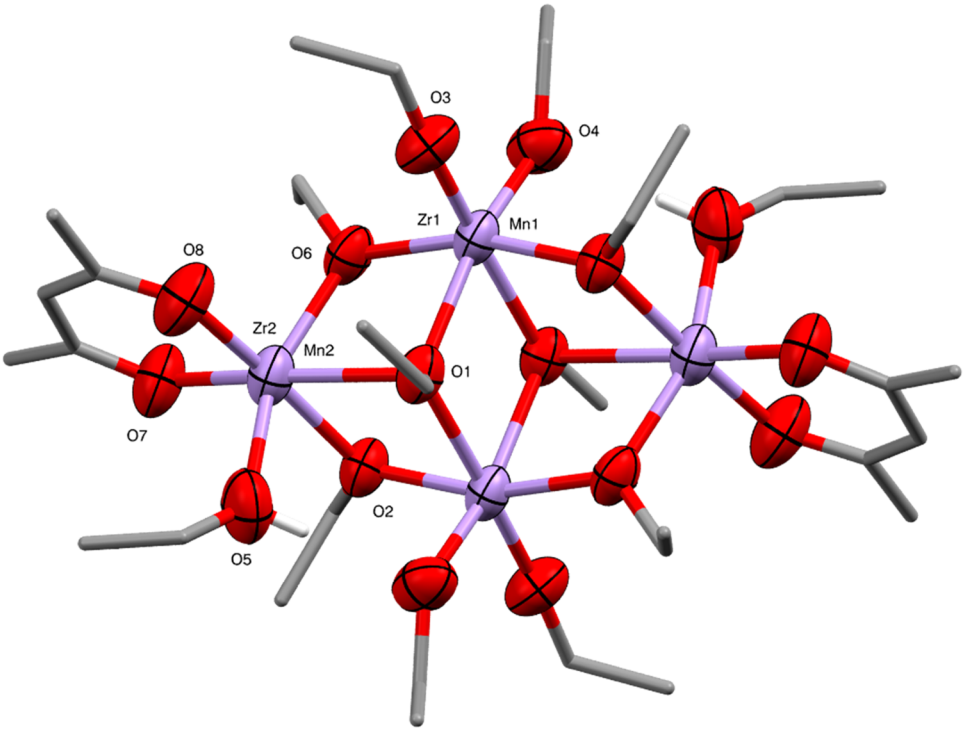

Figure 9. Molecular structure of $Mn_{1.67}Zr_{2.33}(OEt)_{10.66}(acac)_2(EtOH)_{1.34}$ (**7**) (ellipsoids at 50% probability) with H atoms and minor disorder of one ethoxide ligand omitted. The O−H hydrogens of coordinating alcohols are shown. In the crystal examined, the metal position M1 has 9% Mn^{2+} occupancy and 91% Zr^{4+} occupancy, and the metal position M2 has 74% Mn^{2+} occupancy and 26% Zr^{4+} occupancy. Selected bond lengths (Å) and angles (°): M1−O1 2.262(3), M1−O1′ 2.290(3), M1−O2 2.087(3), M1−O3 1.924(4), M1−O4 2.014(4), M1−O6 2.085(4), M2−O1 2.407(3), M2−O2 2.172(3), M2−O5 2.199(5), M2−O6 2.163(4), M2−O7 2.088(4), M2−O8 2.046(4), O−M1−O 74.76(13)−101.96(15), O−M2−O 73.62(12)−101.77(18).

results in ligand substitution to form **5**. Molecules of **5** are based on the $[\{(EtO)_4Zr(\mu_2\text{-}OEt)\}_2]^{2-}$ dianion and are isostructural with the Co^{2+} molecule **3**, with a distorted trigonal-bipyramidal coordination environment for the high-spin d^6 Fe^{2+} ions and a distorted octahedral geometry for the zirconium ions (Figure 7). As for **3**, the presence of the outer trigonal-bipyramidal FeO_5 units results in the greatest degree of distortion from regular octahedral geometry for the central ZrO_6 sites. There have been a number of previous reports of iron-zirconium alkoxides, with the most similar being $FeZr_3O(O^nPr)_{10}(acac)_3$.[34]

A very similar arrangement is also seen in the Cu^{2+} complex $Cu_2Zr_2(OEt)_{10}(acac)_2$ (**6**) (Figure 8), which was obtained from the reaction of $Zr(OEt)_4$, $Cu(acac)_2$, $CuCl_2$, and KOEt in a 2:1:1:2 stoichiometry heated to reflux in toluene and ethanol. While **6** (like **3** and **5**) contains the $[\{(EtO)_4Zr(\mu_2\text{-}OEt)\}_2]^{2-}$ dianion, here the d^9 Cu^{2+} ions have a distorted square-based pyramidal geometry, with the base formed from coordination by two μ_2-ethoxides and one chelating acetylacetonate ligand. In addition to these bonds, there is a long Cu···O interaction with a μ_3-ethoxide (2.543(3) Å, cf. 1.959(4) and 1.964(4) Å for μ_2-ethoxides). From the polyhedral perspective, each outer CuO_5 square-based pyramid joins the central pair of octahedra, again through one triangular face. The adoption of a distorted square pyramidal geometry for Cu^{2+} containing weaker axial interactions has been seen previously in a number of other Cu^{2+} complexes.[35,36]

The adoption of two structural types, both composed of similar $M_2Zr_2O_6$ cores but with the coordinated metal ions (M^{n+}) in different peripheral (**1**, **3**, **5**, and **6**) or central (**2** and **4**) positions (type 1 and type 2, Figure 4), suggests that a combination of factors, such as ionic radii, ionic charge, and crystal field stabilization, influences the observed molecular framework. For example, while there is only a small difference

https://doi.org/10.1021/acs.inorgchem.2c02852
Inorg. Chem. 2022, 61, 19203−19219

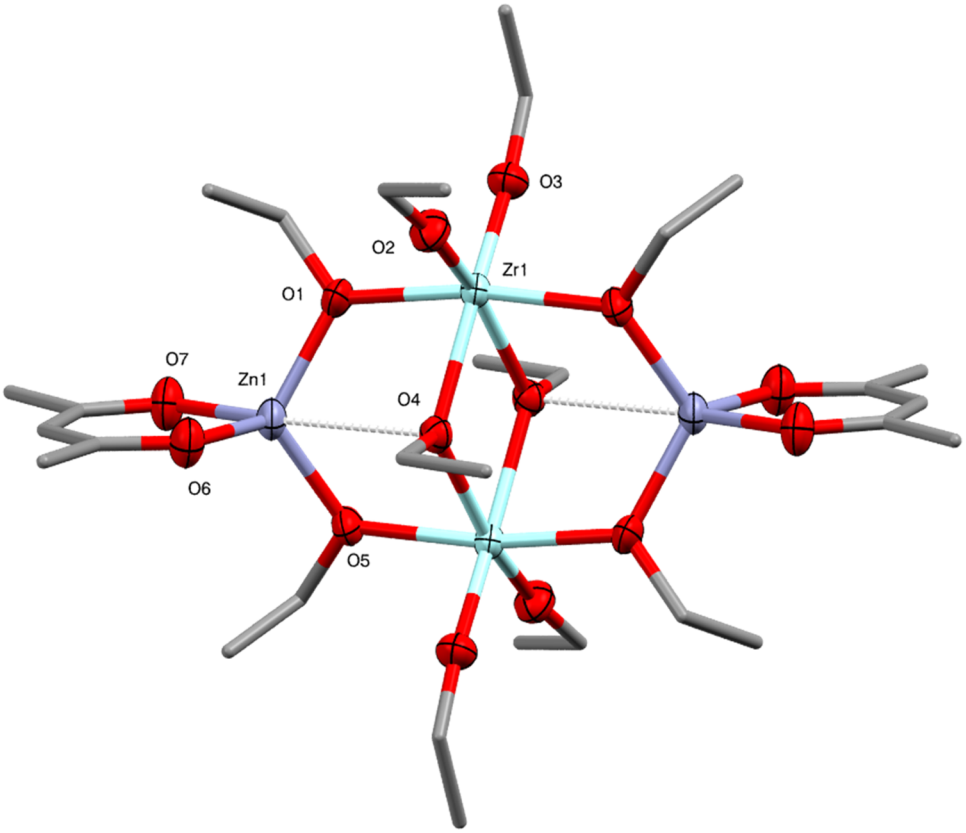

Figure 10. Molecular structure of $Zn_2Zr_2(OEt)_{10}(acac)_2$ (**8**) (ellipsoids at 50% probability) with H atoms omitted. Selected bond lengths (Å) and angles (°): Zn1−O1 1.9300(13), Zn1−O4 2.8013(12), Zn1−O5 1.9354(12), Zn1−O6 1.9596(13), Zn1−O7 1.9851(13), Zr1−O1 2.1401(12), Zr1−O2 1.9358(13), Zr1−O3 1.9396(13), Zr1−O4 2.2001(11), Zr1−O4′ 2.1950(12), Zr1−O5 2.1374(12), O−Zn1−O 95.32(6)-116.59(6), O−Zr1−O 69.73(5)-101.78(6).

in ionic radii between Li^+ (in **1**) and Mg^{2+} (in **2**) (both ≈ 90 pm for octahedral coordination),[37] the key difference is the charge and charge density of the ions. The result is a preference for Li^+ to adopt a four-coordinate pseudo-tetrahedral geometry while octahedral geometries are far more common for Mg^{2+} (i.e., maximizing bond enthalpy). An additional effect underlying the behavior of the transition-metal ions is the difference between crystal field stabilization energies (CFSE) for the various potential coordination environments. It is clear from a consideration of CFSE geometries for the ions (see Table 1) that in the presence of weak-field ligands such as alkoxides, Ni^{2+} has the greatest preference for octahedral geometry (and is found in the central octahedral M site), while Cu^{2+} will prefer square pyramidal. For Fe^{2+} and Co^{2+}, while square pyramidal has the largest CFSE, the trigonal-bipyramidal geometry is observed. This presumably reflects the geometrical match between the alternative coordination polyhedra and the central edge-sharing octahedra.

An indication of the importance of both ionic radius and CFSE is seen in the crystal structure of the Mn^{2+} complex $Mn_{1.67}Zr_{2.33}(OEt)_{10.66}(acac)_2(EtOH)_{1.34}$ (**7**), obtained from the 1:1:2 stoichiometric reaction of $Zr(OEt)_4$, $MnCl_2$, and KOEt heated to reflux in *n*-hexane and ethanol, followed by the addition of one equivalent of acetylacetone. Complex **7** could not be obtained from the reaction of $Zr(OEt)_4$ with $Mn(acac)_2$ alone. The crystal structure of **7** (Figure 9) indicates that the Mn^{2+} and Zr^{4+} ions show site disorder with the peripheral metal positions having 74% Mn^{2+} occupancy and 26% Zr^{4+} occupancy, and the central metal positions have 9% Mn^{2+} occupancy and 91% Zr^{4+} occupancy in the crystal examined. The disorder of the metals in **7** was investigated using ICP-OES to measure the Mn and Zr content. For the formula $Mn_{1.67}Zr_{2.33}(OEt)_{10.66}(acac)_2(EtOH)_{1.34}$, determined from X-ray analysis, the calculated values are 8.8% Mn and 20.4% Zr. The values found experimentally by ICP-OES are 10.4% Mn and 20.0% Zr, showing a greater amount of Mn in the bulk than in the crystallographic model (on a single crystal). The partial occupancy of manganese and zirconium also results in a mixture of ethoxide and ethanol ligands being present in the crystal structure for charge balance. In effect, the complex is part way between the type 1 and 2 arrangements, and this is a reflection of the zero CFSE of the high-spin d^5 electronic configuration of Mn^{2+} in an octahedral (or indeed any) coordination geometry (see Figure 4). Quantitative measures (see Table S2) show that both the M and M′ octahedra in **7** show polyhedral volumes larger than any octahedra in the other complexes, and the M′ site shows the greatest degree of distortion from regular octahedral geometry. This particularly distorted geometry of **7** coincides with the greatest mismatch in ionic radius for Mn^{2+} (97 pm) and Zr^{4+} (86 pm).[37] There are few examples of structurally characterized manganese-zirconium alkoxide, with only two previous examples, and these contained either chloride or nitrogen donor ligands.[38,39] Similar to **2**, the presence of alcohol ligands was investigated using IR spectroscopy. The IR spectrum (Figure S16) has a weak broad signal at about 3100 cm^{-1} attributed to the coordinating alcohol ligands.

https://doi.org/10.1021/acs.inorgchem.2c02852
Inorg. Chem. 2022, 61, 19203−19219

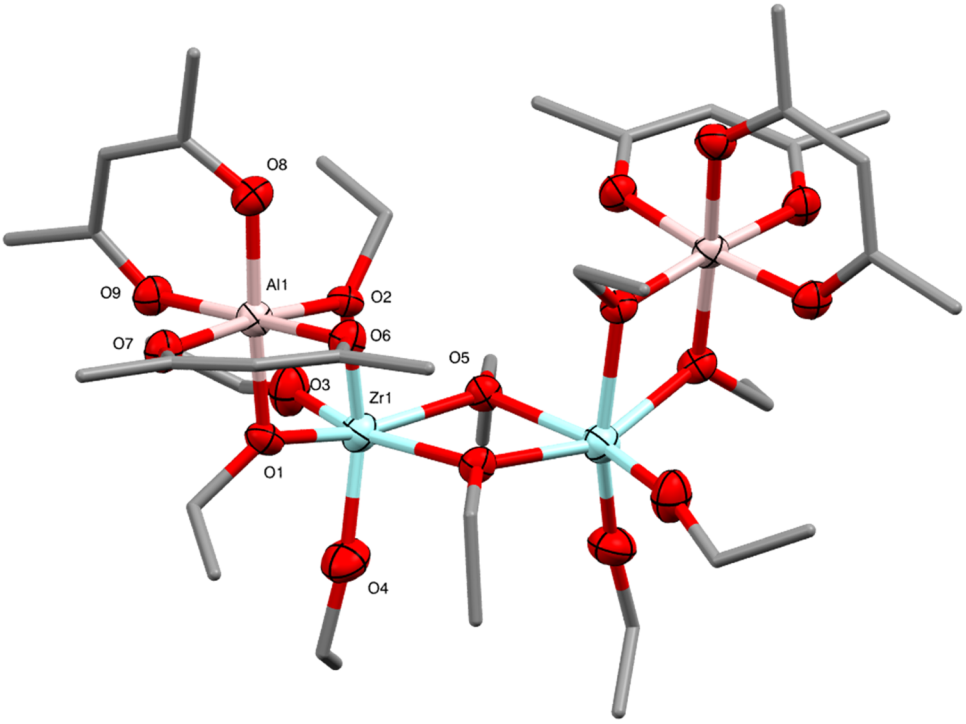

Figure 11. Molecular structure of $Al_2Zr_2(OEt)_{10}(acac)_4$ (**9**) (ellipsoids at 50% probability) with H atoms omitted. Selected bond lengths (Å) and angles (°): Al1−O1 1.885(4), Al1−O2 1.864(4), Al1−O6 1.915(4), Al1−O7 1.906(4), Al1−O8 1.874(5), Al1−O9 1.906(4), Zr1−O1 2.109(4), Zr1−O2 2.161(3), Zr1−O3 1.901(4), Zr1−O4 1.905(5), Zr1−O5 2.105(4), Zr1−O5′ 2.192(4), O−Al1−O 79.10(17)−96.02(18), O−Zr1−O 67.99(15)−105.3(2).

In the Zn^{2+}complex $Zn_2Zr_2(OEt)_{10}(acac)_2$ (**8**) (obtained in a similar synthesis to **7**), steric effects and the relatively small ionic radius of Zn^{2+} are the main structure-directing influences as the d^{10} configuration has no CFSE (see Table 1). Like complexes **1**, **3**, **5**, and **6**, complex **8** is probably best formulated as a $[\{(EtO)_4Zr(\mu_2\text{-}OEt)\}_2]^{2-}$ dianion which (in this case) coordinates two $[Zn(acac)]^+$ fragments at the periphery (i.e., type 1) (Figure 10). Although the coordination geometry of Zn^{2+} appears to be typical four-coordinate, pseudo-tetrahedral, the geometry of **8** actually resembles most closely that of **3** and **5**, which show trigonal-bipyramidal coordination for the M′ site. The additional "axial" contact to atom O4 (2.8013(12) Å, Figure 10) in **8** is long, but it corresponds to bonds seen in **3**, **5**, and **1** (the orientation of the apparent tetrahedron in **8** is quite different from that in **1**). This is the first example of a structurally characterized zinc-zirconium alkoxide not containing Zr−C or Zr−Cl bonds, which are both very air sensitive. In contrast to the other diamagnetic species (**1** and **2**), the room-temperature ^{1}H NMR spectrum of **8** (Figure S6) matches well to the solid-state structure: there are three distinct ethoxide environments in a 2:2:1 ratio and a single acetylacetonate environment.

Finally, moving into the p-block, the Al^{3+} complex $Al_2Zr_2(OEt)_{10}(acac)_4$ (**9**) was synthesized by the reaction of $Zr(OEt)_4$, $Al(OEt)_3$ and acetylacetone in a 1:1:2 stoichiometric ratio. X-ray crystallography revealed a significantly different arrangement to the previous examples (Figure 11). Its spirocyclic structure is composed of a central $[Zr(\mu\text{-}OEt)_2Zr]$ ring connected to two terminal $[Al(\mu\text{-}OEt)_2Zr]$ rings, and is probably best regarded as being composed of a $[\{(EtO)_4Zr(\mu_2\text{-}OEt)\}_2]^{2-}$ dianion (similar to those in complexes **1**, **3**, **5**, **6**, and **8**) which coordinates two terminal $[Al(acac)_2]^+$ cation fragments. This gives the Zr^{4+} and Al^{3+} ions six-coordinate octahedral geometries. The greater distortion of the Zr^{4+} environment appears to result from the chelation of two of the ethoxide groups of the $[\{(EtO)_4Zr(\mu_2\text{-}OEt)\}_2]^{2-}$ dianion on each of the Zr^{4+} ions to the two Al^{3+} ions. The ^{1}H NMR spectrum of **9** (Figure S8) is very complex with a large number of signals, suggesting a number of species in solution at room temperature in dynamic equilibrium. The ^{27}Al NMR spectrum (Figure S10) has two signals (ignoring the background signal) at δ 34.3 and 5.0 ppm, corresponding to five- and six-coordinate aluminum environments, respectively.[40] The ^{1}H NMR spectrum at −50 °C (Figure S13) was little changed from that at room temperature, suggesting that the dynamic processes occurring in solution have low activation energy.

Although $Al_2Zr(O^iPr)_{10}$ was reported previously, being characterized by mass spectrometry and elemental analysis, attempts to crystallize this only resulted in the formation of $Al(O^iPr)_3$.[41] However, the structures of $Al_2Ti(O^iPr)_{10}$ and $Al_2Hf(O^iPr)_{10}$ have been determined by X-ray crystallography.[41,42] In addition, the aluminum-barium-zirconium alkoxide $AlBaZr_2(O^iPr)_{13}(^iPrOH)$ has also been reported.[43] To the best of our knowledge, **9** is the first structurally characterized aluminum−zirconium complex containing only oxygen-based ligands. The absence of reactive Al−C or Al−Cl bonds in **9** which most of the previous examples of aluminum−zirconium complexes have contained makes it a potentially more easily handled SSP for aluminum−zirconium oxide phases.

UV−visible spectroscopy was employed to provide support for the assignment of the oxidation states of the complexes containing paramagnetic transition-metal ions (for which NMR spectroscopy was more challenging). This, however, proved to be relatively uninformative. Complexes **3**, **4**, and **6** all showed d−d transitions in their spectra corresponding to transitions of the M^{2+} ions (Figures S17, S18, and S20). For

https://doi.org/10.1021/acs.inorgchem.2c02852
Inorg. Chem. 2022, 61, 19203−19219

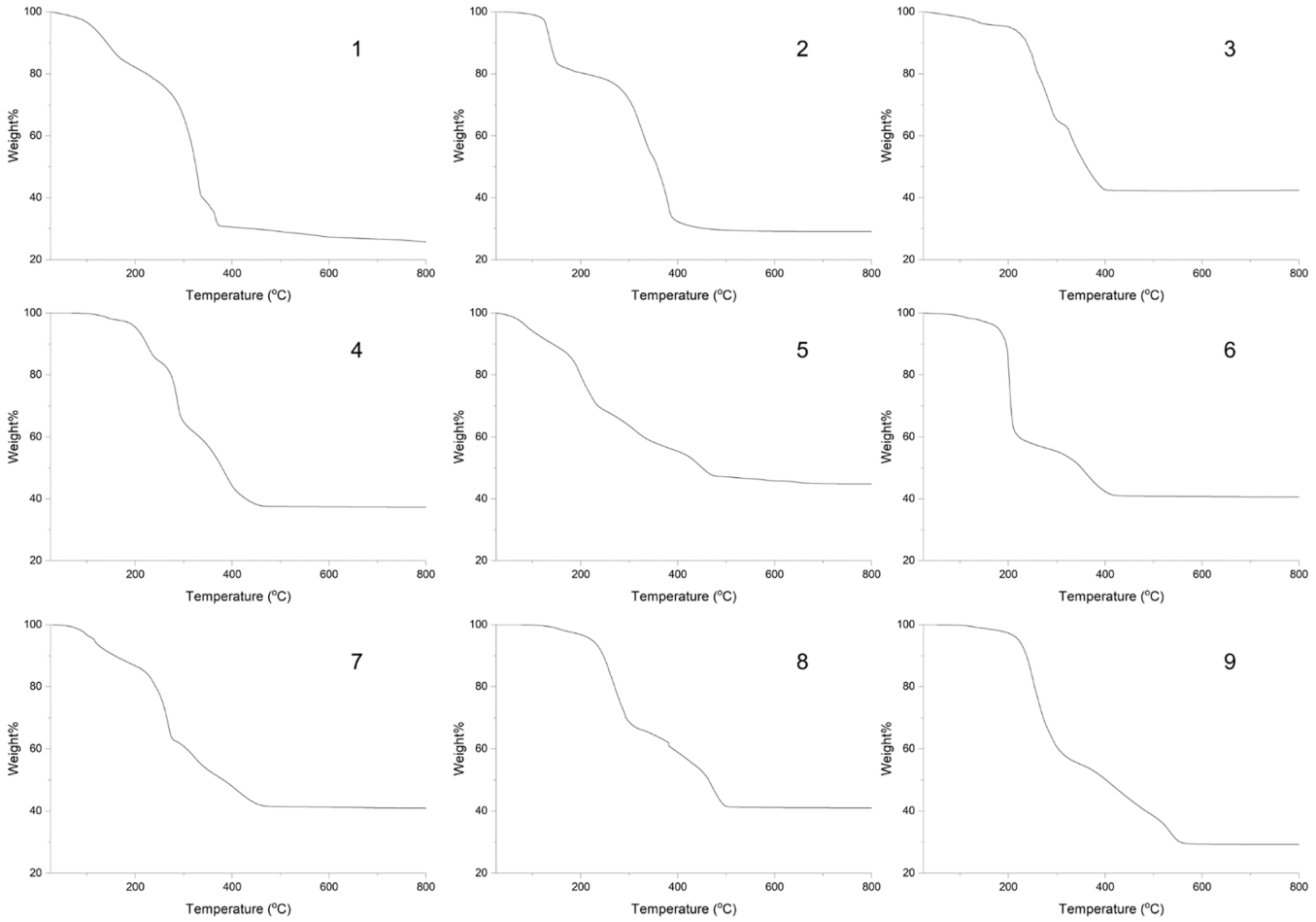

Figure 12. TGA plots of complexes **1**–**9** heated from 25 to 800 °C in air.

complex **5** there are no apparent peaks from d–d transitions (Figure S19), which is unexpected for a high-spin d^6 complex. However, similar behavior has been observed before in comparable iron-titanium alkoxides.[44] The UV–visible spectrum of **7** (Figure S21) does not have any d–d transitions as the Mn^{2+} is high-spin d^5. All of the acac complexes have strong absorption at 400 nm which is assigned to a d to π transition from the metal to the acetylacetonate.[45]

Thermal Decomposition Studies. The thermal decomposition pathways of all of the new compounds were initially tested with thermogravimetric analysis (TGA). For TGA, the samples were heated to 800 °C in air and the weight of the samples was recorded throughout. The TGA traces are shown in Figure 12. Table 2 summarizes the experimental and predicted weight losses.

The thermal decomposition of **1** occurs in two steps with an initial weight loss occurring at 100–200 °C, attributed to the loss of the THF ligands, followed by a second weight loss event at 200–380 °C ascribed to the loss of the *n*-propoxide ligands to leave $Li_2Zr_2O_5$ (experimental remaining weight 30.8%, predicted remaining weight 29.7%). However, continued heating of the material results in a further gradual loss of material, with a final weight of 25.8%. This additional loss is tentatively attributed to the loss of lithium oxide at higher temperatures due to its volatility, resulting in the formation of ZrO_2 (predicted remaining weight 26.5%).[46,47] The behavior of **2** is similar, with a first weight loss of 20% at 120–180 °C, attributed to the loss of four *n*-propanol ligands to give $Mg_2Zr_2(O^nPr)_{12}$, followed by a second weight loss event at 200–450 °C which is due to the loss of the remaining organic ligands to leave $Mg_2Zr_2O_6$ (experimental remaining weight 29.0%, predicted remaining weight 27.7%).

The thermal decomposition of **3** occurs in one combined step with the main loss occurring from 200 to 400 °C. The overall 57.6% weight loss is attributed to the loss of the organic ligands and the formation of $Co_2Zr_2O_6$ (experimental remaining weight 42.4%, predicted remaining weight 41.8%). The TGA trace of **4** has a complicated shape, with multiple overlapping weight loss events. Full decomposition is achieved

Table 2. Experimental and Predicted Weights from the Thermal Decomposition of Complexes 1–9 at 800 °C and the Predicted Products

	remaining weight (%)		
complex	experimental	predicted	predicted product
1	25.8	29.7	$Li_2Zr_2O_5$
2	29.0	27.7	$Mg_2Zr_2O_6$
3	42.4	41.8	$Co_2Zr_2O_6$
4	37.3	37.5	$Ni_2Zr_2O_6$
5	44.8	41.4	$Fe_2Zr_2O_6$
6	40.6	42.3	$Cu_2Zr_2O_6$
7	40.9	38.8	$Mn_{1.67}Zr_{2.33}O_{6.33}$
8	41.0	42.5	$Zn_2Zr_2O_6$
9	29.2	32.2	$Al_2Zr_2O_7$

https://doi.org/10.1021/acs.inorgchem.2c02852
Inorg. Chem. 2022, 61, 19203–19219

Table 3. Summary of the Weight% and Errors of Phases Present from PXRD Rietveld Refinements for Each Decomposition Product after Heating at 800 °C for 4 h in Air (Complex 9 Was Heated to 1000 °C for 4 h in Air)[a]

	phase composition (weight%)				
complex	monoclinic ZrO_2	tetragonal $M_xZr_{1-x}O_{2-\delta}$	cubic $M_xZr_{1-x}O_{2-\delta}$	M phase	other mixed phase
1	52.7(3)				47.3(3) Li_2ZrO_3
2		54.7(14)	26.1(13)	19.2(6) MgO	
3	18.28(13)	45.0(3)		36.75(19) Co_3O_4	
4	10.15(19)	45.9(3)		43.9(2) NiO	
5	12.6(8)	69.5(18)		17.9(11) Fe_2O_3	
6	57.8(7)	1.2(11)		41.0(5) CuO	
7		[a]	[a]	[a]Mn_3O_4	
8	60.20(10)			39.80(10) ZnO	
9		87.9(16)		12.1(16) Al_2O_3	

[a]For complex 7, tetragonal zirconia, cubic zirconia, and Mn_3O_4 are observed, but the composition and structure are unsolved.

at 470 °C, producing $Ni_2Zr_2O_6$ (experimental remaining weight 37.3%, predicted remaining weight 37.5%).

The thermal decomposition of **5** is also complicated. The TGA trace shows at least four weight loss events, with a gradual decrease in weight being observed from room temperature to 700 °C. During loading of the sample, it was noted that **5**, which is red, rapidly turned green upon air exposure, which was attributed to the oxidation of the Fe^{2+} ions to Fe^{3+}. This poor air stability may be partially responsible for the complicated TGA trace. The resulting final weight matches $Fe_2Zr_2O_7$, which corroborates oxidation of Fe^{2+} to Fe^{3+} (experimental remaining weight 44.8%, predicted remaining weight $Fe_2Zr_2O_6$ 41.4%, predicted remaining weight for $Fe_2Zr_2O_7$ 43.1%).

Like **1** and **2**, the thermal decomposition of **6** occurs in two distinct stages. First, a very sharp weight loss of 42% at 200−220 °C, which is attributed to the loss of the ethoxide ligands, and a second stage occurring at 250−420 °C due to the removal of the acetylacetonate ligands to give $Cu_2Zr_2O_6$ (experimental remaining weight 40.6%, predicted remaining weight 42.3%).

A similar picture to **5** is seen in the TGA trace **7**, which is attributed to the more complicated mixed-ligand set and fractional metal composition, with multiple weight loss events occurring between 100 and 470 °C. Based on the formula obtained by X-ray crystallography $(Mn_{1.67}Zr_{2.33}(OEt)_{10.66}(acac)_2(EtOH)_{1.34})$ the expected decomposition product would be $Mn_{1.67}Zr_{2.33}O_{6.33}$ (experimental remaining weight 40.9%, predicted remaining weight 38.8%). The difference between the predicted and observed remaining weights is probably due to variation in the exact Mn:Zr ratio in **7** (i.e., between different crystals in the bulk sample). This discrepancy was confirmed by performing Mn and Zr ICP-OES on **7**.

A two-stage weight loss is observed for **8**. The first weight loss occurs at 150−320 °C and the second at 350−500 °C. These two stages are again attributed to the loss of ethoxide and acetylacetonate ligands, respectively. The final decomposition product has the formula $Zn_2Zr_2O_6$ (experimental remaining weight 41.0%, predicted remaining weight 42.5%).

The thermal decomposition of **9** also has a two-step TGA profile. The first step occurs at 200−320 °C, with the second step occurring at 320−570 °C. Again, these two steps can be linked to the loss of ethoxide and acetylacetonate ligands. This leads to a final composition of $Al_2Zr_2O_7$ (experimental remaining weight 29.2%, predicted remaining weight 32.2%).

Analysis of Decomposition Products. To characterize the products from thermal decomposition, we heated each of the complexes in air at 800 °C for 4 h and performed synchrotron powder X-ray diffraction (PXRD) measurements at the I11 beamline at Diamond Light Source. Detailed composition on analysis was undertaken using Rietveld refinements. The complexes variously phase-segregate into ZrO_2 and the relevant metal oxide and form a mixed-metal phase or a combination of both. The results are summarized in Table 3; refined lattice parameters and phase weight percentages are included in the SI (Table S4 and Figures S22−S30).

Zirconia (ZrO_2) is thermodynamically stable in its monoclinic form (space group $P2_1/c$) below 1170 °C. It is tetragonal ($P4_2/nmc$) from 1170 to 2300 °C and cubic ($Fm\bar{3}m$) above this temperature; zirconium exists in an oxidation state of +4 and forms strong bonds to oxygen, which favors a coordination number of seven or eight. The tetragonal and cubic phases can instead be stabilized at lower temperatures by doping with lower valent ions, which also introduces oxygen vacancies for charge-balancing; yttrium-stabilized cubic zirconia is perhaps the most well known of these compounds.[48−53] Alternatively, when crystallites are below a critical size (found by Shukla et al. to be 30 nm) the high surface area to volume ratio means that oxygen loss at the surface can lead to a sufficient oxygen vacancy concentration to stabilize the tetragonal zirconia phase.[54−56] By choosing the right counterion, we can therefore carefully control the nature of the oxide phases and tailor the lattice parameters and/or oxygen vacancy content to control, e.g., strain/ionic conductivity.

The decomposition products of the Cu (**6**) and Zn (**8**) complexes phase-segregate into monoclinic ZrO_2 and oxide phases of CuO and ZnO, respectively. The preferred coordination is a Jahn−Teller distorted octahedron for d^9 Cu^{2+} and tetrahedral for small d^{10} Zn^{2+} so we can attribute the lack of metal doping in these cases to the very different coordination preferences of the Cu^{2+} and Zn^{2+} ions relative to Zr^{4+}.

The Co (**3**), Ni (**4**), and Fe (**5**) complexes form a doped tetragonal phase with additional monoclinic ZrO_2 and their respective oxide phases Co_3O_4, NiO and Fe_2O_3. This corroborates the TGA data, with some of the Co^{2+} and Fe^{2+} ions being oxidized during heating. The unit cell parameters were correlated with the ionic radii of the metal dopant; the variations of the refined *a* and *c* lattice parameters are shown in Figure 13. There is little change in the *a* lattice parameter for

https://doi.org/10.1021/acs.inorgchem.2c02852
Inorg. Chem. 2022, 61, 19203−19219

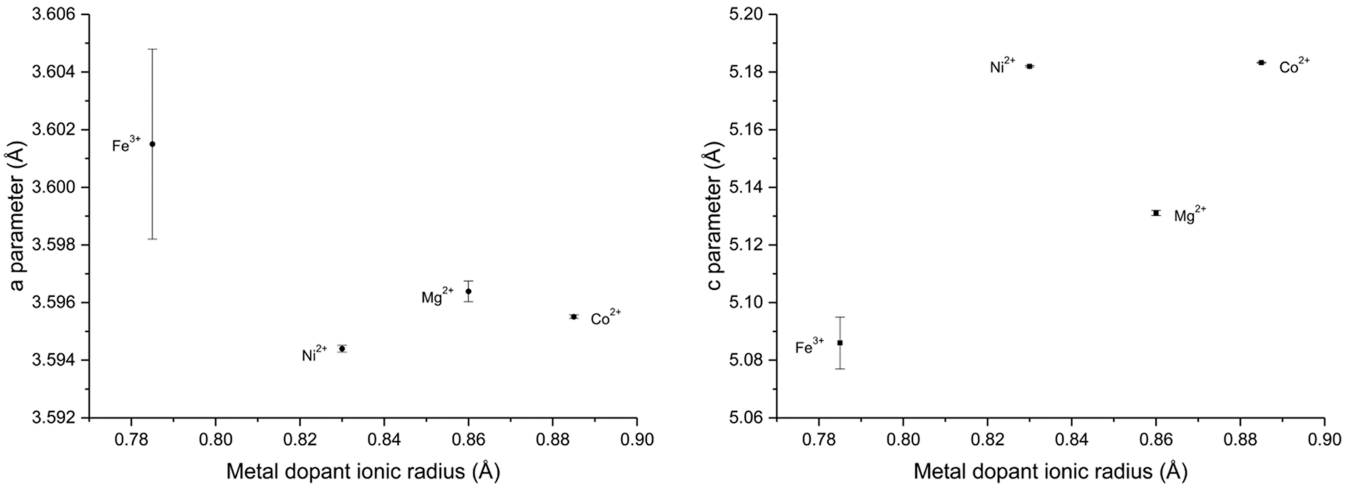

Figure 13. *a* and *c* Parameters with errors for the tetragonal zirconia phases calculated from Rietveld refinement of the PXRD data from the decomposition of the complexes at 800 °C in air for 4 h plotted against the metal dopant ionic radius.

the different metal dopants (0.0071 Å). However, the *c* parameter has a much larger variation (0.09725 Å) and there is a weak positive correlation between the metal dopant ionic radius and the *c* parameter, suggesting doping does affect the *c* parameter. It must be noted that the amount of transition-metal dopant in the tetragonal zirconia does vary for the different dopants, so the absolute change in lattice parameters should only be tentatively analyzed. However, controlling the lattice parameter via doping could be an effective strategy for strain-matching between coatings and electrode materials in any future applications in the coating of battery material.

The Mg complex (**2**) forms a mixture of cubic and tetragonal Mg-doped ZrO_2 and MgO. Due to the similar ionic radii of Mg^{2+} and Zr^{4+} (both ≈ 0.86 Å) and lack of CFSE for both ions, Mg^{2+} ions can easily dope into the zirconia phase, providing significant stabilization for both the cubic and tetragonal phases.[57] The cubic zirconia also receives additional stabilization from forming a solid solution with MgO.[58,59] ZrO_2-MgO nanocomposites are of interest for their high melting points and excellent mechanical properties.[60]

The Mn complex (**7**) forms a mixture of Mn-doped tetragonal ZrO_2, small amounts of tetragonal Mn_3O_4 ($I4_1/amd$), and an additional cubic phase. This cubic phase could be fitted using numerous structural models which do not correspond to known phases containing only Mn and/or Zr with oxygen, so we refine this phase using a Pawley fit with space group $Fm\bar{3}m$. There are also some additional unidentified peaks in the diffraction pattern for which further analysis is required. For the scope of this study, we note simply that the lack of CFSE for Mn^{2+} and Zr^{4+} allows for cation mixing in the decomposition product, analogous to that seen for the molecular structure of **7**.

The refinement of the PXRD data for complex **1** reveals 58% monoclinic Li_2ZrO_3 and 42% monoclinic ZrO_2. This is the only compound to form a non-ZrO_2 based mixed-metal phase.

The thermal decomposition of the Al-containing complex (**9**) at 800 °C resulted in an amorphous product, confirmed by the absence of sharp reflections in the XRD data. This was confirmed by magic-angle spinning ^{27}Al solid-state NMR spectroscopy (Figure S14). The spectrum reveals four-, five-, and six-coordinate aluminum environments similar to that seen for amorphous alumina.[61] This is consistent with previous reactions with alumina-zirconia ceramics, with amorphous samples observed upon heating at 600 °C, but γ-alumina and tetragonal zirconia are observed at 875 °C.[62] Heating to higher temperatures would be required to observe crystalline phases; the increase in the crystallization temperature for zirconia with increasing alumina content has previously been studied.[63] This was evidenced by heating **9** to 1000 °C for 4 h in air, resulting in a mixture of Al_2O_3 and tetragonal ZrO_2 (Figure S31).

The decomposition products of the SSPs were further examined using scanning electron microscopy (SEM) and energy-dispersive X-ray spectroscopy (EDS) to investigate the particle morphology and elemental distribution of the materials heated at 800 °C in air for 4 h. The SEM images reveal a range of different morphologies for the different decomposition products, with most of them forming chunks of material. The EDS maps reveal a uniform distribution of elements in all of the decomposition products, suggesting good mixing of the different phases on the SEM length scale (see Figure S32). This is likely to be due to indistinguishable nanometer-size crystallites, supported by the PXRD refinements, which found crystallite sizes for all of the phases to be in the range of 30–150 nm. This uniform mixing is an important characteristic of SSPs.

CONCLUSIONS

Using a set of similar synthetic methodologies, we have prepared a range of mixed-metal zirconium alkoxide compounds that incorporate metal ions and span the s-, d-, and p-blocks. The study of their solid-state structures has emphasized that the characteristics and coordination preferences of the incorporated metal ions in these zirconium "host" arrangements have a large structure-directing influence. While this conclusion is not new, because of the breadth of these studies we are able to trace the influences of the combined effects of ionic radii, ionic charge, and crystal field stabilization energy across the periodic table. By obtaining a series of these mixed-metal compounds this study provides a range of SSPs for the deposition of a number of metal-zirconium oxide, metal oxide, and zirconium oxide phases. The additional metal ion has a large effect on the zirconia phases formed, being able to stabilize the less thermodynamically stable tetragonal and cubic phases at moderate annealing temperatures. This knowledge may allow the future design of SSPs for specific purposes, where particular zirconia phases are desired. These species

https://doi.org/10.1021/acs.inorgchem.2c02852
Inorg. Chem. 2022, 61, 19203−19219

have the potential to be used in coatings, in particular the coating of battery electrodes to increase cycle lifetime by slowing or preventing degradation. We are continuing these studies by exploring the applications of these and the developing range of zirconium-based SSPs as protective coatings for state-of-the-art cathode materials.

■ ASSOCIATED CONTENT

Supporting Information

The Supporting Information is available free of charge at https://pubs.acs.org/doi/10.1021/acs.inorgchem.2c02852.

(PDF)

Accession Codes

CCDC 2185397−2185398 and 2185400−2185406 contain the supplementary crystallographic data for this paper. These data can be obtained free of charge via www.ccdc.cam.ac.uk/data_request/cif, or by emailing data_request@ccdc.cam.ac.uk, or by contacting The Cambridge Crystallographic Data Centre, 12 Union Road, Cambridge CB2 1EZ, UK; fax: +44 1223 336033.

■ AUTHOR INFORMATION

Corresponding Authors

Clare P. Grey − *Yusuf Hamied Department of Chemistry, University of Cambridge, Cambridge CB2 1EW, United Kingdom; The Faraday Institution, Quad One, Harwell Science and Innovation Campus, Didcot OX11 0RA, United Kingdom;* orcid.org/0000-0001-5572-192X; Email: cpg27@cam.ac.uk

Dominic S. Wright − *Yusuf Hamied Department of Chemistry, University of Cambridge, Cambridge CB2 1EW, United Kingdom; The Faraday Institution, Quad One, Harwell Science and Innovation Campus, Didcot OX11 0RA, United Kingdom;* orcid.org/0000-0002-9952-3877; Email: dsw1000@cam.ac.uk

Authors

Jonathan Slaughter − *Yusuf Hamied Department of Chemistry, University of Cambridge, Cambridge CB2 1EW, United Kingdom; The Faraday Institution, Quad One, Harwell Science and Innovation Campus, Didcot OX11 0RA, United Kingdom;* orcid.org/0000-0002-6401-8547

Chloe Coates − *Yusuf Hamied Department of Chemistry, University of Cambridge, Cambridge CB2 1EW, United Kingdom; The Faraday Institution, Quad One, Harwell Science and Innovation Campus, Didcot OX11 0RA, United Kingdom*

George Phillips − *Yusuf Hamied Department of Chemistry, University of Cambridge, Cambridge CB2 1EW, United Kingdom*

Dipanjana Choudhury − *Yusuf Hamied Department of Chemistry, University of Cambridge, Cambridge CB2 1EW, United Kingdom*

Andrew D. Bond − *Yusuf Hamied Department of Chemistry, University of Cambridge, Cambridge CB2 1EW, United Kingdom;* orcid.org/0000-0002-1744-0489

Complete contact information is available at: https://pubs.acs.org/10.1021/acs.inorgchem.2c02852

Author Contributions

J.S. undertook the synthesis of the molecular complexes, UV−visible spectroscopy, and TGA measurements. J.S., D.C., and C.C. undertook NMR studies. A.D.B. carried out X-ray crystallography and analysis of the solid-state structures. C.C. and G.P. performed PXRD and SEM/EDS measurements. G.P. undertook IR measurements. D.S.W. and C.P.G. supervised the work on this project. All authors were involved in the writing of the paper.

Notes

The authors declare no competing financial interest.

■ ACKNOWLEDGMENTS

J.S., C.C., C.P.G., and D.S.W. thank the Faraday Institution (grant numbers FIRG001 and FIRG024) for funding. PXRD measurements were carried out at the I11 beamline at Diamond Light Source, for which the authors acknowledge the award of a Block Allocation Grant (CY28349). They also thank Dr. Chris O'Keefe for help running solid-state NMR spectroscopy.

■ REFERENCES

(1) Fang, S.; Bresser, D.; Passerini, S. Transition Metal Oxide Anodes for Electrochemical Energy Storage in Lithium- and Sodium-Ion Batteries. *Adv. Energy Mater.* **2020**, *10*, No. 1902485.

(2) Jose, R.; Thavasi, V.; Ramakrishna, S. Metal Oxides for Dye-Sensitized Solar Cells. *J. Am. Ceram. Soc.* **2009**, *92*, 289−301.

(3) Védrine, J. Heterogeneous Catalysis on Metal Oxides. *Catalysts* **2017**, *7*, 341.

(4) Meixner, H.; Lampe, U. Metal Oxide Sensors. *Sensors Actuators B Chem.* **1996**, *33*, 198−202.

(5) Schünemann, F. H.; Galárraga-Vinueza, M. E.; Magini, R.; Fredel, M.; Silva, F.; Souza, J. C. M.; Zhang, Y.; Henriques, B. Zirconia Surface Modifications for Implant Dentistry. *Mater. Sci. Eng. C* **2019**, *98*, 1294−1305.

(6) Anderson, J.; Van de Walle, C. G. Fundamentals of Zinc Oxide as a Semiconductor. *Reports Prog. Phys.* **2009**, *72*, No. 126501.

(7) Liu, W.; Li, X.; Xiong, D.; Hao, Y.; Li, J.; Kou, H.; Yan, B.; Li, D.; Lu, S.; Koo, A.; Adair, K.; Sun, X. Significantly Improving Cycling Performance of Cathodes in Lithium Ion Batteries: The Effect of Al_2O_3 and $LiAlO_2$ Coatings on $LiNi_{0.6}Co_{0.2}Mn_{0.2}O_2$. *Nano Energy* **2018**, *44*, 111−120.

(8) Hao, Z.; Yang, S.; Niu, J.; Fang, Z.; Liu, L.; Dong, Q.; Song, S.; Zhao, Y. A Bimetallic Oxide $Fe_{1.89}Mo_{4.11}O_7$ Electrocatalyst with Highly Efficient Hydrogen Evolution Reaction Activity in Alkaline and Acidic Media. *Chem. Sci.* **2018**, *9*, 5640−5645.

(9) Li, M.; Xiong, Y.; Liu, X.; Bo, X.; Zhang, Y.; Han, C.; Guo, L. Facile Synthesis of Electrospun MFe_2O_4 (M = Co, Ni, Cu, Mn) Spinel Nanofibers with Excellent Electrocatalytic Properties for Oxygen Evolution and Hydrogen Peroxide Reduction. *Nanoscale* **2015**, *7*, 8920−8930.

(10) Colmenares, J. C.; Aramendía, M. A.; Marinas, A.; Marinas, J. M.; Urbano, F. J. Synthesis, Characterization and Photocatalytic Activity of Different Metal-Doped Titania Systems. *Appl. Catal. A Gen.* **2006**, *306*, 120−127.

(11) Wilke, K.; Breuer, H. D. The Influence of Transition Metal Doping on the Physical and Photocatalytic Properties of Titania. *J. Photochem. Photobiol. A Chem.* **1999**, *121*, 49−53.

(12) Lu, H.; Wright, D. S.; Pike, S. D. The Use of Mixed-Metal Single Source Precursors for the Synthesis of Complex Metal Oxides. *Chem. Commun.* **2020**, *56*, 854−871.

(13) Hubert-Pfalzgraf, L. G. Metal Alkoxides and β-diketonates as Precursors for Oxide and Non-oxide Thin Films. *Appl. Organomet. Chem.* **1992**, *6*, 627−643.

(14) Rao, C. N. R. Chemical Approaches to the Design of Oxide Materials. *Pure Appl. Chem.* **1994**, *66*, 1765−1772.

(15) Lu, H.; Andrei, V.; Jenkinson, K. J.; Regoutz, A.; Li, N.; Creissen, C. E.; Wheatley, A. E. H.; Hao, H.; Reisner, E.; Wright, D. S.; Pike, S. D. Single-Source Bismuth (Transition Metal) Polyox-

ovanadate Precursors for the Scalable Synthesis of Doped $BiVO_4$ Photoanodes. *Adv. Mater.* **2018**, *30*, No. 1804033.
(16) Tahir, A. A.; Mazhar, M.; Hamid, M.; Wijayantha, K. G. G. U.; Molloy, K. C. Photooxidation of Water by $NiTiO_3$ Deposited from Single Source Precursor $[Ni_2Ti_2(OEt)_2(\mu\text{-}OEt)_6(acac)_4]$ by AACVD. *Dalton Trans.* **2009**, 3674.
(17) Wei, Z.; Han, H.; Filatov, A. S.; Dikarev, E. V. Changing the Bridging Connectivity Pattern within a Heterometallic Assembly: Design of Single-Source Precursors with Discrete Molecular Structures. *Chem. Sci.* **2014**, *5*, 813−818.
(18) Schipper, F.; Bouzaglo, H.; Dixit, M.; Erickson, E. M.; Weigel, T.; Talianker, M.; Grinblat, J.; Burstein, L.; Schmidt, M.; Lampert, J.; Erk, C.; Markovsky, B.; Major, D. T.; Aurbach, D. From Surface ZrO_2 Coating to Bulk Zr Doping by High Temperature Annealing of Nickel-Rich Lithiated Oxides and Their Enhanced Electrochemical Performance in Lithium Ion Batteries. *Adv. Energy Mater.* **2018**, *8*, No. 1701682.
(19) Izumi, K.; Murakami, M.; Deguchi, T.; Morita, A.; Tohge, N.; Minami, T. Zirconia Coating on Stainless Steel Sheets from Organozirconium Compounds. *J. Am. Ceram. Soc.* **1989**, *72*, 1465−1468.
(20) Pol, S. V.; Pol, V. G.; Seisenbaeva, G.; Kessler, V. G.; Gedanken, A. Stabilization of Metastable Face-Centered Cubic Cobalt and the Tetragonal Phase of Zirconia by a Carbon Shell: Reaction under Autogenic Pressure at Elevated Temperature of $CoZr_2(acac)_2(OiPr)_8$. *Chem. Mater.* **2004**, *16*, 1793−1798.
(21) Petrus, R.; Chomiak, K.; Utko, J.; Wilk-Kozubek, M.; Lis, T.; Cybińska, J.; Sobota, P. Convenient Route to Heterometallic Group 4-Zinc Precursors for Binary Oxide Nanomaterials. *Inorg. Chem.* **2020**, *59*, 8108−8120.
(22) Ehsan, M. A.; Khaledi, H.; Arifin, Z.; Mazhar, M. Synthesis and Characterization of a Heterobimetallic Cu-Zr Complex for Deposition of 1:1 $CuZrO_3$-CuO Composite Thin Films. *Polyhedron* **2015**, *98*, 190−195.
(23) Seisenbaeva, G. A.; Gohil, S.; Kessler, V. G. Influence of Heteroligands on the Composition, Structure and Properties of Homo- and Heterometallic Zirconium Alkoxides. Decisive Role of Thermodynamic Factors in Their Self-Assembly. *J. Mater. Chem.* **2004**, *14*, 3177−3190.
(24) Dubey, R. K.; Singh, A.; Mehrotra, R. C. Synthesis and Characterization of Copper(II) Bis(Dizirconium-Ennea-Alkoxides). *Polyhedron* **1987**, *6*, 427−433.
(25) Seisenbaeva, G. A.; Gohil, S.; Kessler, V. G. Molecular Design Approach to a Highly Soluble and Volatile Bimetallic Alkoxide of Late Transition Metal and Zirconium. Synthesis, X-Ray Single Crystal and Mass-Spectral Study of $NiZr_2(acac)(O^iPr)_9$. *Inorg. Chem. Commun.* **2007**, *10*, 94−96.
(26) Fulmer, G. R.; Miller, A. J. M.; Sherden, N. H.; Gottlieb, H. E.; Nudelman, A.; Stoltz, B. M.; Bercaw, J. E.; Goldberg, K. I. NMR Chemical Shifts of Trace Impurities: Common Laboratory Solvents, Organics, and Gases in Deuterated Solvents Relevant to the Organometallic Chemist. *Organometallics* **2010**, *29*, 2176−2179.
(27) Beswick, M. A.; Mosquera, M. E. G.; Wright, D. S. Structural Direction by the Dominant Metal. *J. Chem. Soc. - Dalton Trans.* **1998**, 2437−2443.
(28) Clegg, W.; Harrington, R. W. CCDC 2042280: Experimental Crystal Structure Determination. *CSD Commun.*, 2020.
(29) Petrus, R.; Drąg-Jarząbek, A.; Utko, J.; Bykowski, D.; Lis, T.; Sobota, P. Molecular Routes to Group IV Magnesium and Calcium Nanocrystalline Ceramics. *Inorg. Chem.* **2017**, *56*, 11365−11374.
(30) Ibers, J. A. Crystal and Molecular Structure of Titanium (IV) Ethoxide. *Nature* **1963**, *197*, 686−687.
(31) Spijksma, G. I.; Seisenbaeva, G. A.; Fischer, A.; Bouwmeester, H. J. M.; Blank, D. H. A.; Kessler, V. G. The Molecular Composition of Non-Modified and acac-Modified Propoxide and Butoxide Precursors of Zirconium and Hafnium Dioxides. *J. Sol-Gel Sci. Technol.* **2009**, *51*, 10−22.
(32) Schmid, R.; Mosset, A.; Galy, J. New Precursors in the Chemistry of IVB Transition Metal Alkoxides. III. Synthesis and Structure of $Zr_2Co_2(\mu_3\text{-}OC_3H_7)_2(\mu_2\text{-}OC_3H_7)_4(OC_3H_7)_4(acetylacetone)_2$. *Acta Crystallogr. Sect. C Cryst. Struct. Commun.* **1991**, *47*, 750−752.
(33) Kessler, V. G.; Spijksma, G. I.; Seisenbaeva, G. A.; Håkansson, S.; Blank, D. H. A.; Bouwmeester, H. J. M. New Insight in the Role of Modifying Ligands in the Sol-Gel Processing of Metal Alkoxide Precursors: A Possibility to Approach New Classes of Materials. *J. Sol-Gel Sci. Technol.* **2006**, *40*, 163−179.
(34) Schmid, R.; Ahamdane, H.; Mosset, A. New Precursors in the Chemistry of IVB Transition Metal Alkoxides V. Synthesis and Molecular Structure of $Zr_3Fe(\mu_4\text{-}O)(\mu_2\text{-}OC_3H_7)_6(OC_3H_7)_4(acac)_3$. *Inorganica Chim. Acta* **1991**, *190*, 237−240.
(35) Kim, K. M.; Kim, K. H.; Kang, T. Y.; Park, J. S.; Song, R.; Jun, M. J. The Non-Templated Empty Cavity and Its Selective Anion Binding despite Having Similar Shapes. *Chem. Commun.* **2003**, *3*, 1410−1411.
(36) Yagishita, S.; Himegi, A.; Kanazashi, K.; Ohishi, T.; Ishikawa, R.; Hamaguchi, T.; Kawata, S. Structural Transformations of Layered Structures Constructed from Cu(II)-Chloranilate Monomer Compounds. *Dalton Trans.* **2017**, *46*, 2966−2973.
(37) Shannon, R. D. Revised Effective Ionic Radii and Systematic Studies of Interatomic Distances in Halides and Chalcogenides. *Acta Crystallogr., Sect. A* **1976**, *32*, 751−767.
(38) Sobota, P.; Utko, J.; John, L.; Jerzykiewicz, L. B.; Drég-Jarzábek, A. Unexpected Cyclopentadienyl/Alkoxo Ligand Exchange in Titano- and Zirconocene. New Opportunities. *Inorg. Chem.* **2008**, *47*, 7939−7941.
(39) Malaestean, I. L.; Speldrich, M.; Ellern, A.; Baca, S. G.; Kögerler, P. Heterometal Expansion of Oxozirconium Carboxylate Clusters. *Dalton Trans.* **2011**, *40*, 331−333.
(40) Benn, R.; Rufińska, A. High-Resolution Metal NMR Spectroscopy of Organometallic Compounds. *Angew. Chem. Int. Ed. Engl.* **1986**, *25*, 861−881.
(41) Turevskaya, E. P.; Berdyev, D. V.; Turova, N. Y.; Starikova, Z. A.; Yanovsky, A. I.; Struchkov, Y. T.; Belokon, A. I. Bimetallic Alkoxides of Aluminium-Hafnium and Aluminium-Zirconium. X-Ray Structure of $Al_2Hf(OPr^i)_{10}$. *Polyhedron* **1997**, *16*, 663−670.
(42) Tudyka, S. S.; Pflanz, K.; Aldinger, F.; Borrmann, H.; Fischer, P.; Brunner, H. Synthese Und Charakterisierung Eines Neuen Gemischten Titan-Aluminium-Alkoxids. *Z. Anorg. Allg. Chem.* **1997**, *623*, 1163−1167.
(43) Heidemann, T.; Mathur, S. Three at a Time: Step by Step to Heterotermetallic Molecules. *Inorg. Chem.* **2017**, *56*, 234−240.
(44) Eslava, S.; Goodwill, B. P. R.; McPartlin, M.; Wright, D. S. Extending the Family of Titanium Heterometallic-Oxo-Alkoxy Cages. *Inorg. Chem.* **2011**, *50*, 5655−5662.
(45) Barnum, D. W. Electronic Absorption Spectra of Acetyl-Acetonato Complexes-I: Complexes with Trivalent Transition Metal Ions. *J. Inorg. Nucl. Chem.* **1961**, *21*, 221−237.
(46) Sata, T. High-Temperature Vaporization of Li_2O Component from Solid Solution $Li_xNi_{1-x}O$ in Air. *Ceram. Int.* **1998**, *24*, 53−59.
(47) Sata, T. Vaporization Rate of Li_2O from Double Oxides. *J. Ceram. Soc. Japan* **1998**, *106*, 660−664.
(48) Bocanegra-Bernal, M. H.; De La Torre, S. D. Phase Transitions in Zirconium Dioxide and Related Materials for High Performance Engineering Ceramics. *J. Mater. Sci.* **2002**, *37*, 4947−4971.
(49) Vest, R. W.; Tallan, N. M.; Tripp, W. C. Electrical Properties and Defect Structure of Zirconia: I, Monoclinic Phase. *J. Am. Ceram. Soc.* **1964**, *47*, 635−640.
(50) Kumar, A.; Rajdev, D.; Douglass, D. L. Effect of Oxide Defect Structure on the Electrical Properties of ZrO_2. *J. Am. Ceram. Soc.* **1972**, *55*, 439−445.
(51) Jin, X. J. Martensitic Transformation in Zirconia Containing Ceramics and Its Applications. *Curr. Opin. Solid State Mater. Sci.* **2005**, *9*, 313−318.
(52) Chevalier, J.; Gremillard, L.; Virkar, A. V.; Clarke, D. R. The Tetragonal-Monoclinic Transformation in Zirconia: Lessons Learned and Future Trends. *J. Am. Ceram. Soc.* **2009**, *92*, 1901−1920.

https://doi.org/10.1021/acs.inorgchem.2c02852
Inorg. Chem. 2022, 61, 19203−19219

(53) Gupta, T. K.; Bechtold, J. H.; Kuznicki, R. C.; Cadoff, L. H.; Rossing, B. R. Stabilization of Tetragonal Phase in Polycrystalline Zirconia. *J. Mater. Sci.* **1977**, *12*, 2421−2426.
(54) Shukla, S.; Seal, S. Mechanisms of Room Temperature Metastable Tetragonal Phase Stabilisation in Zirconia. *Int. Mater. Rev.* **2005**, *50*, 45−64.
(55) Garvie, R. C. The Occurrence of Metastable Tetragonal Zirconia as a Crystallite Size Effect. *J. Phys. Chem. A* **1965**, *69*, 1238−1243.
(56) Juárez, R.; Lamas, D. G.; Lascalea, G. E.; Walsöe de Reca, N. E. Synthesis and Structural Properties of Zirconia-Based Nanocrystalline Powders and Fine-Grained Ceramics. *Defect Diffus. Forum* **2000**, *177−178*, 1−26.
(57) Sim, S. M.; Stubican, V. S. Phase Relations and Ordering in the System ZrO_2-MgO. *J. Am. Ceram. Soc.* **1987**, *70*, 521−526.
(58) Duran, P.; Rodriguez, J. M.; Recio, P. The ZrO_2-Rich Region of the ZrO_2-MgO System. *J. Mater. Sci.* **1991**, *26*, 467−472.
(59) Rondão, A. I. B.; Muccillo, E. N. S.; Muccillo, R.; Marques, F. M. B. On the Electrochemical Properties of Mg-PSZ: An Overview. *J. Appl. Electrochem.* **2017**, *47*, 1091−1113.
(60) Keerthana, L.; Sakthivel, C.; Prabha, I. MgO-ZrO_2 Mixed Nanocomposites: Fabrication Methods and Applications. *Mater. Today Sustainable* **2019**, *3−4*, No. 100007.
(61) Sarou-Kanian, V.; Gleizes, A. N.; Florian, P.; Samélor, D.; Massiot, D.; Vahlas, C. Temperature-Dependent 4-, 5- and 6-Fold Coordination of Aluminum in MOCVD-Grown Amorphous Alumina Films: A Very High Field ^{27}Al-NMR Study. *J. Phys. Chem. C* **2013**, *117*, 21965−21971.
(62) Low, I. M.; McPherson, R. Crystallization of Gel-Derived Alumina and Alumina-Zirconia Ceramics. *J. Mater. Sci.* **1989**, *24*, 892−898.
(63) Dahl, G. T.; Döring, S.; Krekeler, T.; Janssen, R.; Ritter, M.; Weller, H.; Vossmeyer, T. Alumina-Doped Zirconia Submicro-Particles: Synthesis, Thermal Stability, and Microstructural Characterization. *Materials* **2019**, *12*, 2856.

https://doi.org/10.1021/acs.inorgchem.2c02852
Inorg. Chem. 2022, 61, 19203−19219